

Discovery of Two Ultra-Diffuse Galaxies with Unusually Bright Globular Cluster Luminosity Functions via a Mark-Dependently Thinned Point Process (MATHPOP)

DAYI (DAVID) LI (李大一)^{1, 2, *} GWENDOLYN M. EADIE^{1, 2, 3} PATRICK E. BROWN^{1, 4} WILLIAM E. HARRIS^{1, 5}, ROBERTO G. ABRAHAM^{1, 6} PIETER VAN DOKKUM^{1, 7} STEVEN R. JANSSENS^{1, 8} SAMANTHA C. BEREK^{1, 2, 3, 6, †} SHANY DANIELI^{1, 9, ‡} AARON J. ROMANOWSKY^{1, 10, 11} AND JOSHUA S. SPEAGLE (沈佳士)^{1, 2, 3, 6}

¹Department of Statistical Sciences, University of Toronto, 700 University Avenue, Toronto, ON M5G 1Z5 Canada

²Data Sciences Institute, University of Toronto, 700 University Avenue, Toronto, ON, M5G 1Z5 Canada

³David A. Dunlap Department of Astronomy & Astrophysics, University of Toronto, 50 St George St, Toronto, ON, M5S 3H4 Canada

⁴Center for Global Health Research, St. Michael's Hospital, 30 Bond Street, Toronto, ON M5B 1W8 Canada

⁵Department of Physics and Astronomy, McMaster University, Hamilton, ON L8S 4M1, Canada

⁶Dunlap Institute for Astronomy & Astrophysics, University of Toronto, 50 St George St, Toronto, ON, M5S 3H4 Canada

⁷Department of Astronomy, Yale University, New Haven, CT 06511, USA

⁸Centre for Astrophysics and Supercomputing, Swinburne University, Hawthorn VIC 3122, Australia

⁹Department of Astrophysical Sciences, 4 Ivy Lane, Princeton University, Princeton, NJ 08544, USA

¹⁰Department of Physics & Astronomy, San José State University, One Washington Square, San Jose CA 95192, USA

¹¹Department of Astronomy and Astrophysics, University of California Santa Cruz, 1156 High Street, Santa Cruz, CA 95064, USA

ABSTRACT

We present MATHPOP, a novel method to infer the globular cluster (GC) counts in ultra-diffuse galaxies (UDGs) and low-surface brightness galaxies (LSBGs). Many known UDGs have a surprisingly high ratio of GC number to surface brightness. However, standard methods to infer GC counts in UDGs face various challenges, such as photometric measurement uncertainties, GC membership uncertainties, and assumptions about the GC luminosity functions (GCLFs). MATHPOP tackles these challenges using the mark-dependent thinned point process, enabling joint inference of the spatial and magnitude distributions of GCs. In doing so, MATHPOP allows us to infer and quantify the uncertainties in both GC counts and GCLFs with minimal assumptions. As a precursor to MATHPOP, we also address the data uncertainties coming from the selection process of GC candidates: we obtain probabilistic GC candidates instead of the traditional binary classification based on the color–magnitude diagram. We apply MATHPOP to 40 LSBGs in the Perseus cluster using GC catalogs from a *Hubble Space Telescope* imaging program. We then compare our results to those from an independent study using the standard method. We further calibrate and validate our approach through extensive simulations. Our approach reveals two LSBGs having GCLF turnover points much brighter than the canonical value with Bayes' factor being ~ 4.5 and ~ 2.5 , respectively. An additional crude maximum-likelihood estimation shows that their GCLF TO points are approximately 0.9 mag and 1.1 mag brighter than the canonical value, with p -value $\sim 10^{-8}$ and $\sim 10^{-5}$, respectively.

Keywords: Globular Clusters (656); Ultra-Diffuse Galaxies (940); LSBG (940); Point Processes (1915); Astrostatistics (1882); Bayesian Statistics (1900)

1. INTRODUCTION

Ultra-diffuse galaxies (UDGs) are a class of extended low-surface brightness galaxies (LSBGs) first found in abundance in the Coma cluster by van Dokkum et al. (2015) using the Dragonfly Telephoto Array (Abraham & van Dokkum 2014). van Dokkum et al. (2015) defined UDGs through their effective radii ($R_e > 1.5$ kpc)

Corresponding author: Dayi (David) Li
 dayi.li@mail.utoronto.ca

* Data Sciences Institute Doctoral Fellow,
 CANSSI Ontario Multi-disciplinary Doctoral Trainee

† Data Sciences Institute Doctoral Fellow

‡ NASA Hubble Fellow

and g -band central surface brightness ($\mu_{0,g} > 24.5$ mag arcsec $^{-2}$). Subsequently, thousands of UDGs were found in galaxy clusters (e.g. Yagi et al. 2016; Wittmann et al. 2017; Janssens et al. 2019; Lim et al. 2020) but also in low-density environments (e.g., Martínez-Delgado et al. 2016; Román et al. 2019; Forbes et al. 2019; Forbes et al. 2020; Danieli et al. 2020).

Despite their faintness, UDGs seem to have a surprisingly large number of globular clusters (GCs). It is found that UDGs have on average 5–7 times more GCs than other typical galaxies of the same luminosity (Peng & Lim 2016; van Dokkum et al. 2017; Amorisco et al. 2018; Lim et al. 2018; Danieli et al. 2021). Some even seem to have GC numbers that rival the Milky Way (van Dokkum et al. 2016; van Dokkum et al. 2017), despite being almost 100 times fainter.

It is well-established that there is a monotonic relationship between the stellar mass of the galaxy and the total numbers or mass of the GC population (e.g., Harris et al. 2013; De Souza et al. 2015; Berek et al. 2023), at least for Milky-Way mass galaxies and above. For lower mass galaxies, such as dwarfs, the relationship is somewhat unclear (Eadie et al. 2022; Berek et al. 2023) since the majority of them have very few or no GCs. Where UDGs fit into this observed relationship is still unclear, and the apparent mismatch between the stellar mass and GC population in UDGs poses an interesting challenge to current models of galaxy formation (Lim et al. 2018; van Dokkum et al. 2019c; Saifollahi et al. 2022; Danieli et al. 2022; Ferré-Mateu et al. 2023; Forbes & Gannon 2024; Buzzo et al. 2024).

UDGs and their GC populations may also provide insight into the nature of dark matter (Hu et al. 2000; Hui et al. 2017; Wasserman et al. 2019; van Dokkum et al. 2019a). Multiple theoretical and observational studies have found that there is a relationship between the halo mass of the galaxy and the mass of the GC system (Hudson et al. 2014; Harris et al. 2015; El-Badry et al. 2019; Bastian et al. 2020; Chen & Gnedin 2023). However, kinematic studies of UDGs have found cases that appear to be extreme outliers from these relations. For example, Dragonfly-44 seems to be made almost entirely of dark matter (van Dokkum et al. 2016), while NGC 1052-DF2 and DF4 have little to no dark matter (Van Dokkum et al. 2018; van Dokkum et al. 2019b; Shen et al. 2023). Despite the apparent extremity of the inferred dark matter content of these UDGs, they all have significant GC populations.

Within the above context, accurate characterizations of GC systems in UDGs are crucial to furthering our understanding of galaxy formation and the nature of dark matter. Thus, inferring the GC counts (N_{GC}) of

UDGs has been a central theme in UDG studies (e.g., Peng & Lim 2016; Amorisco et al. 2018; Lim et al. 2018, 2020; Carlsten et al. 2022; Saifollahi et al. 2022, Janssens et al. 2024).

Despite having a larger number of GCs than expected, UDGs/LSBGs still have relatively low N_{GC} ($\lesssim 100$) compared to the most massive galaxies in the Universe. Moreover, the majority of UDGs identified to date reside in rather distant galaxy clusters. At these distances, even powerful telescopes such as the *Hubble Space Telescope* struggle to fully probe down to the turnover (TO) point of the globular cluster luminosity function (GCLF; Harris et al. 2014). The combination of small GC counts and limited resolution at large distances makes it difficult to accurately infer and quantify the uncertainty of N_{GC} in UDGs. The absence of a statistically robust and rigorous GC counting method further exacerbates these challenges.

In many studies (see e.g., Peng & Lim 2016; van Dokkum et al. 2017; Lim et al. 2018; Saifollahi et al. 2022, Janssens et al. 2024, and others), different methods and assumptions were used when estimating N_{GC} of UDGs at large distances, although these methods generally involve the following steps (with some small variations). First, point sources are extracted from astronomical images. Next, GC candidates are identified using the colors and magnitudes of the point sources. Based on the GC candidates, GCs within a certain radius (either predetermined or fitted) from the center of a UDG are then counted. Next, corrections are applied to account for GCs located at larger radii. The count is then adjusted by subtracting an estimated background GC count to correct for chance alignments. Finally, unobserved faint GCs are accounted for by making assumptions about the shape of the GCLF.

Although simple and efficient, the standard method presents various challenges that can impact the accuracy and the uncertainty quantification of N_{GC} for UDGs:

- The photometric uncertainties of GC magnitudes and colors increase exponentially as one approaches the detection limit of the images (e.g., Harris 2023). Such measurement uncertainties can propagate into the binary selection of GC candidates. Although various studies (e.g., Peng & Lim 2016; Harris et al. 2020, Janssens et al., 2024) mitigate this issue by removing sources with high measurement uncertainty, potentially useful information in the data may be discarded, which may impact the analysis.
- GC membership is uncertain; given a GC candidate, we do not know if it belongs to a UDG, a

nearby bright galaxy, or the intergalactic medium (IGM). Intuitively, GCs near the center of a galaxy are more likely to be its member, and the GC spatial distribution in a galaxy is needed to quantify such uncertainty. However, without the GC membership, it is difficult to quantify the GC spatial distribution. How does one quantify such uncertainty heavily affects both N_{GC} and GCLF estimates. For example, many studies (e.g., Peng & Lim 2016; van Dokkum et al. 2017; Saifollahi et al. 2022) estimated the GCLFs of UDGs using only the GC candidates within $1 - 1.5R_e$ (after a simple constant background subtraction) due to the significant GC membership uncertainty at larger radii. Naturally, this procedure ignores a large amount of data outside the chosen radii and if there are other nearby bright galaxies, a constant background subtraction will bias the results.

- The chosen radius within which GCs are counted is often fixed and based on the assumption that it contains a certain fraction of N_{GC} in a UDG (e.g., van Dokkum et al. 2017; Lim et al. 2018, Janssens et al. 2024 in prep). This assumption may not always hold, and the associated uncertainties are seldom addressed.
- To correct for unobserved GCs, various studies adopt a fixed GCLF (e.g. van Dokkum et al. 2016; Lim et al. 2018; Amorisco et al. 2018; Carlsten et al. 2022; Saifollahi et al. 2022, Janssens et al. 2024) where it is either the canonical GCLF or inferred from the stacked GC data within a study. However, the GCLF can vary depending on the host galaxies (e.g., Villegas et al. 2010), and the GCLFs of different galaxies may not be the same as that of the ensemble population. Ideally, we would like to infer the GCLF directly from the data for each individual galaxy, but as mentioned, this is challenging if GC membership is unknown, and is further complicated by the photometric measurement uncertainties. Moreover, recent observations (Shen et al. 2021; Janssens et al. 2022; Romanowsky et al. 2024, Tang et al. submitted to ApJ) of UDGs NGC1052-DF2, DF4, DGSAT I, and FCC 224 suggest that their GCLFs are weighted towards more luminous GCs than expected from the canonical GCLF. This challenges the widely accepted universality of the GCLF. If true, then this has consequences for any study of UDG GC systems.
- In many cases (e.g., Lim et al. 2018, 2020; Carlsten et al. 2022), the background subtraction step

produces negative N_{GC} estimates or confidence intervals extending into the negative range, which is unphysical.

Given these complexities, N_{GC} estimates can vary significantly between different studies of the same UDG. For example, van Dokkum et al. (2016); van Dokkum et al. (2017); Lim et al. (2018); Saifollahi et al. (2022); Forbes & Gannon (2024) produced N_{GC} estimates for Dragonfly-44 that range from 20^{+6}_{-5} (Saifollahi et al. 2022) to 94^{+25}_{-20} (van Dokkum et al. 2016). Hence, there is an urgent need for a more statistically robust and rigorous methodology to improve the reliability of N_{GC} estimates in UDG.

The methods proposed by Amorisco et al. (2018) and Carlsten et al. (2022) represent significant steps toward accurately estimating N_{GC} of UDGs. Amorisco et al. (2018) constructed a mixture model to address the GC membership uncertainties while Carlsten et al. (2022) considered the uncertainty on whether a source is indeed a GC. However, certain limitations persist in their approaches. For example, both Amorisco et al. (2018); Carlsten et al. (2022) assumed a fixed GCLF, which may not account for the variability of GCLFs. Carlsten et al. (2022) encountered the challenges of negative GC count estimates and confidence intervals. Additionally, neither of these studies accounted for the measurement uncertainties of GC magnitudes and colors. While these studies have offered valuable insights into the challenges of accurately estimating N_{GC} of UDGs, they also underscore the need for further methodological improvements.

In this paper, we introduce a novel approach to address the challenges of GC counting in UDGs/LSBGs via a hierarchical Bayesian point process model. Point process models have recently garnered attention within the astrophysics community (e.g., Stein et al. 2015; Li & Barmby 2021; Li et al. 2022; Fan et al. 2023; Li et al. 2024). As exemplified in Li et al. (2022, 2024), point processes are natural frameworks to model the data generating process of GCs when trying to discover UDGs through their GC populations. In this work, we further exploit the power of point processes to address the problem of counting the GCs in UDGs.

We propose a Bayesian MArk-dependently THinned POint Process (MATHPOP; Myllymäki 2009) to jointly model the spatial distribution and the magnitude distribution of GCs. MATHPOP is a special point process model where some points are removed (thinned) with probabilities depending on the locations and/or marks (characteristics) of the points. Such a framework seamlessly fits into the context of GC counting: the marks of points are the magnitudes of the GCs, and the un-

observed faint GCs are the thinned points in a point process due to their magnitudes and/or locations.

We also take into account the uncertainty when selecting GC candidates. We use two finite mixture models (Benaglia et al. 2009; Chauveau & Hoang 2016) to perform clustering on the color–magnitude data of point sources. Using the clustering results, we construct a probabilistic catalog of GC candidates while incorporating the measurement uncertainties of the point sources.

The Bayesian approach of our method integrates the probabilistic GC catalog with our MATHPOP framework. The joint Bayesian modeling of the GC point pattern and their magnitudes enables us to comprehensively address all associated uncertainties. The point process model gives us the ability to quantify the uncertainty in GC membership assignment, which then provides us the means to model the GCLFs of individual UDGs. In turn, we can also include photometric measurement uncertainty without excluding data. Moreover, through the use of a point process, we avoid unphysical, negative estimates of N_{GC} and instead obtain the probability that a UDG has no GCs.

Our paper, which both introduces our method and applies it to 40 LSBGs in the Perseus cluster, is organized as follows. Section 2 introduces the GC catalogs we construct for analysis. Section 3 describes the MATHPOP framework and our model. Section 4 contains the results and analysis for the 40 LSBGs in Perseus as well as an extensive simulation study. Section 5 includes discussions and conclusions. A publicly available R package for MATHPOP is at https://github.com/davidolohowski/MATHPOP_R_pkg. Users can also access the MATHPOP web-page at <https://ddavidli.com/MATHPOP/> for quick MATHPOP tutorials as well as code to reproduce the results in this paper.

2. DATA AND BACKGROUND

2.1. GC Candidates Selection

We apply our method to data from the Program for Imaging of the PERseus cluster (PIPER; Harris et al. 2020) survey. The survey was conducted by the *Hubble Space Telescope* (*HST*) with its on-board Advanced Camera for Surveys (ACS) and Wide Field Camera 3 (WFC3). The target region for observation is the Perseus galaxy cluster, for which we adopt a distance of 75 Mpc as in Harris et al. (2020).

The survey consists of 15 imaging visits, with each visit containing two images within the Perseus region, one captured by ACS and the other by WFC3. These images were taken using the F475W and F814W filters with ACS, and the F475X and F814W filters with WFC3. ACS images span an area of $\sim 76 \times 76 \text{ kpc}^2$ at

the Perseus distance, while WFC3 images have an area of $\sim 62 \times 62 \text{ kpc}^2$. Each image is designated with its visit number and the camera, e.g., V6-ACS is the image obtained by ACS during the Visit 6. 10 of the 15 imaging visits target the outer region of the Perseus cluster at locations of known UDGs, and we use these 10 imaging visits (20 images) to construct the GC catalog.

We note that Janssens et al. 2024 (hereafter J24) conducted an independent study on the GC populations of UDGs via the standard approach using the same PIPER imaging material. We hereafter refer to the GC counting method in J24 as the standard approach. We also apply our method to their GC catalog for comparison, as the GC selection criteria in J24 are different from ours.

In terms of UDGs/LSBGs, the PIPER survey covers 50 LSBGs with 33 of them from Wittmann et al. (2017) (designated W) and 17 from visual inspection of archival CFHT/Megacam imaging by A. Romanowsky (designated R). 23 of the 50 LSBGs meet the strict definition of a UDG (van Dokkum et al. 2015) and the rest are either slightly more compact or brighter in surface brightness.

In the next section, we present the procedure to construct our GC catalog, and then briefly discuss the GC catalog from J24.

2.1.1. Point Source Selection and A Probabilistic GC Catalog

A major advantage for selecting GCs in Perseus is that, at the 75 Mpc distance, the great majority of GCs appear unresolved (with half-light diameters less than $0.02''$), enabling the use of photometric software codes like DAOPHOT and DOLPHOT. In the original PIPER study (Harris et al. 2020), DAOPHOT (Stetson 1987) was used for photometry.

For our study, the 20 images covering the outer Perseus fields were measured anew with DOLPHOT (Dolphin 2000, 2016). The procedure to extract the point source list in each field is described in more detail in Harris (2023). Briefly, an initial list was constructed with all objects in the field detected in the deepest filter (here F814W), and magnitudes measured by PSF (point spread function) fitting. The list was then culled by including only objects successfully measured in both filters. Next, clearly non-stellar objects of any kind were removed, as determined by the `sharp` and `chi` DOLPHOT parameters and magnitude-dependent exclusion boundaries (see particularly the analysis of the central Perseus field for NGC 1275 by Harris 2023). A careful manual inspection was performed to confirm and finalize the selection of the point sources. As a final note, the data from images V7-WFC3 and V8-WFC3 were omitted from our analysis, as DOLPHOT could not

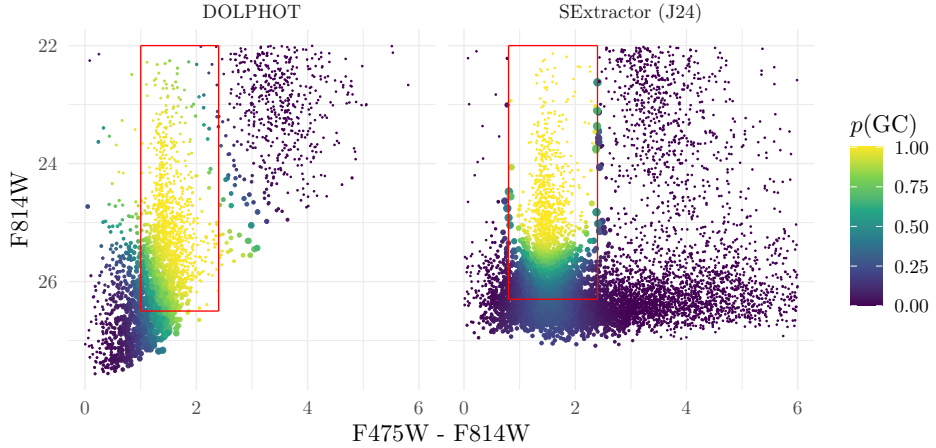


Figure 1. Color-magnitude diagram of a portion of sources obtained from DOLPHOT and SExtractor (J24). The red boxes indicate the typical selection region of the GCs. The color is the probability that a source is a GC, as obtained from finite-mixture models (see text). The size of the points in both panels indicates the uncertainty of the estimated probability.

converge to solutions as it failed to coordinate-match the list of point sources found in these two fields. Due to the convergence issue, 40 of the 50 LSBGs in the PIPER survey were covered in our DOLPHOT data, with one LSB galaxy, W7, being observed in V12-ACS and partially observed in V14-ACS. The structural properties of the LSBGs were obtained by J24, and we use their results for subsequent analyses. Our GC candidate catalog is thus constructed based on a total of 18 images at different locations in the Perseus region.

The final photometric lists are in the natural *HST* filter magnitudes in Vegamag. For the WFC3 data, the measurements in F475X were transformed to the equivalent F475W (ACS) (see [Harris et al. 2020](#)). Foreground extinctions were removed for all measurements and individual fields, as given in [Harris et al. \(2020\)](#).

The left panel of Figure 1 shows the color-magnitude diagram (CMD) for a portion of extracted point sources (50% of data are randomly selected due to memory constraints). Because normal, old GCs occupy a well-determined range of magnitudes and colors, corresponding to their luminosities and metallicities, a typical GC selection method is to construct a box that generously encloses the expected color and magnitude range for GCs (see [Harris et al. 2020](#), for details). This approach is represented by the red box in the left panel of Figure 1, which contains likely GCs. This approach is a binary selection, in that point sources are identified as likely GCs or not.

Rather than applying a strict binary classification to identify GCs, we adopt a probabilistic approach. The motivation is obvious: GCs certainly do not reside in a box in the CMD. Not only will some GCs reside outside the box, but the box will also contain some number

of contaminants (foreground stars or faint, small background galaxies). Moreover, measurement uncertainties in the color-magnitude data can be significant at fainter levels, which can have a strong impact on the binary selection results. Therefore, we apply a non-parametric multivariate finite mixture model ([Benaglia et al. 2009](#); [Chauveau & Hoang 2016](#)) to the color-magnitude data to estimate the probability that a source is a GC. The details of obtaining the probability are given in Appendix B.1.

The color of each point in the left panel of Figure 1 shows the estimated probability that a source is a GC, while the size represents the uncertainty of the estimates. For example, a point that is yellow and small has a high probability of being a GC, with low uncertainty. Note that we have excluded sources with $F814W < 22.0$ mag and $F475W - F814W < 0.0$ mag to stabilize the clustering algorithm. These sources are also highly unlikely to be GCs.

2.1.2. Comparison to GC Catalog from J24

The selection process for the GC catalog by J24 was rather similar to ours (see J24 for more details). Briefly, SExtractor ([Bertin & Arnouts 1996](#)) was run in dual-image mode on all images using the F814W images, after removing the light profile of LSBGs using the best-fit Imfit ([Erwin 2015](#)) model. A point source catalog was then constructed using the concentration parameter C_{5-12} , the F814W magnitude difference measured in 5 and 12 pixel diameter apertures¹. Lastly, GC candidates were selected from point sources using a

¹ Note that J24 used a different set of science images with a final pixel scale of 0.03''.

binary selection criterion in (extinction corrected) magnitude and color of $21.5 < \text{F814W} < 26.3$ mag, and $0.8 < \text{F475W} - \text{F814W} < 2.4$ mag. The faint limit of the selection criterion corresponds to the canonical GCLF TO point. The right panel of Figure 1 shows the CMD of point sources from J24 (only showing 50% of sources), while the red box in the figure shows the GC selection criteria by J24.

We also construct a probabilistic GC catalog using the J24 point source list. However, since the point source catalog in J24 contains significantly more contaminants than ours at fainter levels (see Appendix B.2 for a detailed account of the existence of these contaminants), the method used for our data has issues in separating GCs from contaminants using the color–magnitude data. Thus, we use a different method to obtain the probabilistic catalog from the one used for our data. In short, we consider a two-component parametric mixture model to cluster the color–magnitude data of sources that pass the color cuts by J24 (see Appendix B.2). As in the left panel of Figure 1, the color and size of points in the right panel represent the estimated probability and uncertainty.

The difference between the probabilities shown in Figure 1 for the two datasets is mainly due to identification of point sources in each approach. SExtractor is more permissive than DOLPHOT for what is considered a point source in that SExtractor only considered point sources successfully detected in F814W filter, while DOLPHOT considered those detected in both filters. Thus, at faint levels, the J24 catalog contains more contaminants than our catalog, which explains the significant difference in GC probabilities between the two catalogs around (1.5 mag, 26 mag) in the CMDs. With only color–magnitude data, no clustering algorithm can confidently separate GCs from contaminants in this region, owing to the large numbers of contaminants (see Appendix B.2 for further details).

2.2. GC Removal due to Completeness Fraction

The main challenge in estimating GC counts in UDGs is that faint GCs are unobservable because of the detection limits in the images. The proportion of detectable GCs is usually a function of their magnitudes m , quantified by the completeness fraction, $f(m)$. More generally, the completeness fraction is a function of both the magnitude m and the local background surface brightness, which is a function of location s , since brighter background light around the centers of host galaxies makes it more difficult to detect faint objects (see Harris 2023, for examples). However, in our case we assume $f(m, s) = f(m)$, since the background stellar light from

UDGs/LSBGs is extremely faint and the images avoid the brightest core region of the Perseus cluster.

To determine $f(m)$, artificial star tests (AST) (cf. Harris et al. 2020; Harris 2023) were performed and the point source recovery rate was measured in the range of $20.0 - 31.75$ mag for F814W and $23 - 31.5$ mag for F475W. $f(m)$ is obtained by fitting the AST results with a logistic function (see e.g., Harris et al. 2016; Harris et al. 2020):

$$f(m) = 1/(1 + \exp(a(m - m_0))),$$

where a controls the rate of decrease in $f(m)$ as m increases and m_0 is the 50% completeness limit. The fitted parameters a and m_0 for the two filters F475W and F814W from the AST are included in Appendix A.

2.3. Measurement Uncertainty in Magnitude

As the brightness of a GC approaches the image detection limit, the uncertainty σ_M in its measured magnitude increases. Typically, $\sigma_M(m_t)$ is a function of the true GC magnitude m_t , and characterized by an exponential function (Harris 2023):

$$\sigma_M(m_t) = \beta_0 \exp(\beta_1(m_t - m_1)), \quad (1)$$

where β_0, β_1, m_1 are free parameters. These parameters are again determined through AST, where measurement uncertainties are derived by comparing the true magnitudes of injected artificial stars with their measured magnitudes from DOLPHOT. During model fitting, we set $m_1 = 25.5$ mag (roughly the central value of the magnitude range being considered in the AST), and the fitted values from the AST for β_0, β_1 are given in Appendix A.

3. METHODS

In this section, we introduce our methodology, MATHPOP, for inferring GC counts using point processes. While traditional methods to infer GC counts require fragmented steps and various assumptions, modeling GCs through point processes is a coherent approach that keeps assumptions to a minimum. Readers familiar with point process models may skip to Section 3.3, where we introduce the concept of a mark-dependently thinned point process. For quick reference, Table 1 contains the list of model parameters and mathematical notation.

3.1. Spatial Point Process

The simplest spatial point process is a homogeneous Poisson process (HPP) with a constant intensity $\lambda \geq 0$,

	Type	Unit	Meaning
\mathbf{x}	Data	-	Observed GC point pattern data
m	Data	mag	Observed GC magnitude data in F814W
\mathcal{S}	Constant	-	Observation window (image field of view)
\mathbf{s}	Random variable	(kpc, kpc)	Unrealized random location of GC
s	Data/Place-holder	(kpc, kpc)	Location of an observed GC/a fixed location in \mathcal{S}
π	Function	-	Probability/probability density function (p.d.f.)
\mathbf{X}, \mathbf{X}'	Random processes	-	Thinned (\mathbf{X}) and unthinned (\mathbf{X}') GC point processes
Λ, Λ'	Latent functions	kpc^{-2}	Intensity of thinned (Λ) and unthinned (Λ') GC point processes
λ_0	Model Parameter	kpc^{-2}	Intensity of unthinned GC point process in IGM.
N_{GC}	Latent variable	-	Number of GCs in a galaxy
λ	Model Parameter	-	Rate parameter for the mean number of GCs in a galaxy
c	Constant	(kpc, kpc)	Central location of a galaxy
R_h	Model Parameter	kpc	Half-number radius of a GC system
R_e	Constant	kpc	Effective radius of a galaxy
α	Model Parameter	-	Sérsic index of a GC system
ϑ	Constant	radian	Orientation angle of a GC system
e	Constant	-	Ellipticity (aspect ratio) of a GC system
M	Random variable	mag	Measured magnitudes in F814W of GCs
M_{true}	Latent variable	mag	True magnitudes in F814W of GCs
$f(m)$	Fixed function	-	Completeness fraction
$\sigma_M(m)$	Fixed function	mag	Measurement uncertainty of GC magnitudes
$\rho(s)$	Function	-	Spatial thinning probability
μ_{TO}	Model Parameter	mag	GCLF TO point in F814W (not adjusted for distance)
σ	Model Parameter	mag	GCLF dispersion
$\phi(m; \mu_{\text{TO}}, \sigma^2)$	Latent Function	-	True GCLF
$\psi(m; \mu_{\text{TO}}, \sigma^2)$	Latent Function	-	GCLF with measurement uncertainty
$\mathcal{N}_f(\mu_{\text{TO}}, \sigma^2)$	Distribution	mag	Distribution of observed GC magnitudes in F814W
Ψ_f	Latent variable	-	Proportion of GCs that are observable given $f(m)$ and GCLF

Table 1. Parameters and notations used in this paper. Subscripts and superscripts are dropped for simplicity. Note that model parameters are quantities we directly infer about the model. Random variables and processes are quantities directly related to data generation. Latent variables and functions are intermediate unknown quantities determined by other quantities such as model parameters and random variables.

independent of locations s . If the intensity $\lambda(s)$ changes with s , then we instead have an inhomogeneous Poisson process (IPP). In our application, the intensity is the mean point count per unit area, and we model the GCs as points generated by an IPP, as follows.

We begin by considering the simplest scenario where we have observed locations $\mathbf{x} = \{s_i\}_{i=1}^n$ of GCs in one UDG. We assume that \mathbf{x} is generated by a GC point process $\mathbf{X} = \{\mathbf{s}_i\}_{i=1}^n$, where \mathbf{X} resides in a bounded observation window $\mathcal{S} \subseteq \mathbb{R}^2$, which is the field of view of an image. The main characteristic of \mathbf{X} is its intensity function $\lambda(s) \geq 0, s \in \mathcal{S}$.

Importantly, we purposely define \mathbf{X} for the observed GCs only. In this way, we can account for incomple-

ness in GC counts through a thinned point process, described next.

3.2. Thinning of Point Process

The process \mathbf{X} defined in Section 3.1 only produces a GC point pattern \mathbf{x} that we can observe. We are actually interested in the *true* GC point process \mathbf{X}' with intensity $\lambda'(s)$ that generates all GCs in a UDG. An advantage of the point process framework is that it can map the true point process \mathbf{X}' to the observed point process \mathbf{X} through an operation called *thinning*.

Thinning is the random removal of points in the point process \mathbf{X}' . Typically, thinning occurs according to a *thinning probability* $\rho(s) \in [0, 1]$ that depends on s . If points $\mathbf{s}_i \in \mathbf{X}'$ are thinned *independently* with probabil-

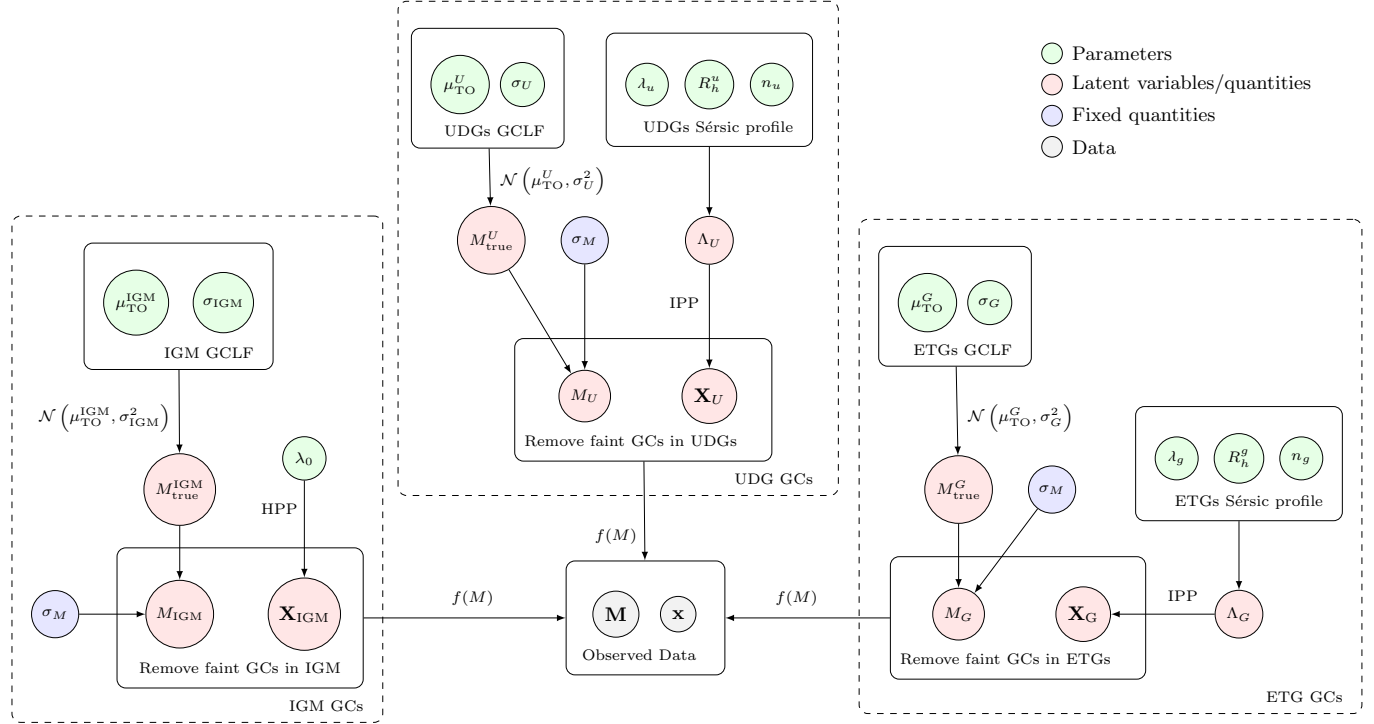


Figure 2. Graphical representation for the data generating process of the observed GC point pattern \mathbf{x} and magnitudes \mathbf{M} under MATHPOP. \mathbf{x} and \mathbf{M} come from independent unions of three different branches of data generating processes for GCs in IGM, UDGs, and luminous early type galaxies.

ity $1 - \rho(\mathbf{s}_i)$, such an operation is called independent- $\rho(s)$ thinning. The resulting thinned point process \mathbf{X} is another point process with intensity $\lambda(s) = \lambda'(s)\rho(s)$. Additionally, if \mathbf{X}' is a Poisson process, then \mathbf{X} is also a Poisson process. Thus, if $\rho(s)$ is known, we can directly infer the property of \mathbf{X}' (what we want) using \mathbf{X} (what we observe).

3.3. Mark-Dependently Thinned Point Process

In our application, we not only have the observed positions of the GCs, but also have measurements of their magnitudes. Under point process terminology, the magnitudes \mathbf{M} are called the *mark*, meaning they are a characteristic attached to the points. Therefore, a natural way to analyse this type of data is with a *marked point process* (Myllymäki 2009; Myllymäki & Penttinen 2009).

We can model the observed GCs with a marked point process $(\mathbf{X}, \mathbf{M}) \subset \mathcal{D}$ where $\mathcal{D} = \mathcal{S} \times \mathcal{M} \subset \mathbb{R}^2 \times \mathbb{R}$. The intensity is $\lambda_M(s, m)$, where (\mathbf{X}, \mathbf{M}) is obtained from thinning $(\mathbf{X}', \mathbf{M}')$. Thus, the thinning can depend on both GC locations and magnitudes.

The intensity function of $(\mathbf{X}', \mathbf{M}')$ is now $\lambda'_M(s, m) \geq 0$ for $(s, m) \in \mathcal{D}$, and we can write

$$\lambda'_M(s, m) = \lambda'(s)\pi'(m | s) = \lambda'(s)\pi'(m) \quad (2)$$

where $\lambda'(s)$ is the intensity of the unmarked point process \mathbf{X}' and $\pi'(m | s)$ is the conditional probability den-

sity function (p.d.f.) of the mark given the location. For our problem, $\pi'(m | s) = \pi'(m)$ is the Globular Cluster Luminosity Function (GCLF). The dependence on s is dropped since GC magnitudes generally do not depend on the GC locations in a galaxy.

Since $\lambda_M(s, m)$ is still the intensity function of a marked point process, we have

$$\lambda_M(s, m) = \lambda(s)\pi(m | s), \quad (3)$$

where $\lambda(s)$ is the intensity of \mathbf{X} and $\pi(m | s)$ is the p.d.f. of the observed GC magnitudes \mathbf{M} at location s .

We next define a new thinning probability $t(s, m) \in [0, 1]$ that can depend on both the location and the magnitude. We assume that the *observed* GC process (\mathbf{X}, \mathbf{M}) is obtained from independent $t(s, m)$ -thinning of the *true* GC process $(\mathbf{X}', \mathbf{M}')$. An immediate implication is that

$$\pi(m | s) = \frac{\pi'(m)t(s, m)}{\int \pi'(m)t(s, m)dm} \triangleq \frac{\pi'(m)t(s, m)}{\Pi'_t(s)}. \quad (4)$$

The above is effectively applying $t(s, m)$ as a truncation function to $\pi'(m | s)$ which produces the magnitude distribution of observed GCs. In our problem, we will assume $t(s, m) = f(m)$, i.e., the thinning of unobserved GCs is caused by the completeness fraction $f(m)$.

Therefore, we have

$$\pi(m | s) = \pi(m) = \frac{\pi'(m)f(m)}{\int \pi'(m)f(m)dm} \triangleq \frac{\pi'(m)f(m)}{\Pi'_f}. \quad (5)$$

The spatial thinning probability $\rho(s)$ that determines whether a GC at location s is removed or not is then obtained by marginalizing m . Hence,

$$\rho(s) = \int \pi'(m)f(m)dm = \Pi'_f, \quad (6)$$

and

$$\lambda(s) = \lambda'(s)\Pi'_f. \quad (7)$$

3.4. Model for GC Point Process

Following the MATHPOP framework in Section 3.3, we now present our complete model. For visual aid, Figure 2 shows a graphical representation of our complete model. Since we are using a probabilistic catalog of GCs, we require additional model structures to include the uncertainty of GC candidates. For coherency, we leave the details of these additional structures in Appendix C.

3.4.1. Modeling the Unmarked GC Point Process

We first focus on the modelling of the unmarked GC point processes \mathbf{X} (observed, thinned) and \mathbf{X}' (true). Let $\Lambda(s) \geq 0$ be the intensity of \mathbf{X} , and $\Lambda'(s) \geq 0$ the intensity of \mathbf{X}' .

Note that \mathbf{X} and \mathbf{X}' are more complicated than we have described in Section 3.3 because the GCs may come from different sub-populations. We assume \mathbf{X}' are independent unions of GC point processes from the following three distinct GC sub-populations:

GCs in the Intergalactic Medium (IGM):

Denoted by \mathbf{X}'_{IGM} with intensity $\Lambda'_{\text{IGM}}(s)$.

GCs in Luminous Early-Type Galaxies (ETGs):

Denoted by \mathbf{X}'_G with intensity $\Lambda'_G(s)$.

GCs in UDGs/LSBGs:

Denoted by \mathbf{X}'_U with intensity $\Lambda'_U(s)$.

By the independent union assumption, we have

$$\mathbf{X}' = \mathbf{X}'_{\text{IGM}} \cup \mathbf{X}'_G \cup \mathbf{X}'_U, \quad (8)$$

and

$$\Lambda'(s) = \Lambda'_{\text{IGM}}(s) + \Lambda'_G(s) + \Lambda'_U(s). \quad (9)$$

The modeling assumptions for GC point processes in each of the above three sub-populations are as follows:

IGM: \mathbf{X}'_{IGM} is a HPP with intensity $\Lambda'_{\text{IGM}}(s) \equiv \lambda_0 > 0$ (see Harris et al. 2020; Li et al. 2024, for a detailed justification).

ETGs and UDGs/LSBGs: \mathbf{X}'_G and \mathbf{X}'_U are IPPs.

We model the GC intensity in ETGs and UDGs/LSBGs using the Sérsic profile (Harris 1991; Wang et al. 2013; Peng & Lim 2016; van Dokkum et al. 2017; Saifollahi et al. 2022):

$$\text{Sérsic}(s; \lambda, R_h, \alpha) = \frac{\lambda b_\alpha^{2\alpha}}{2\pi R_h^2 \alpha \Gamma(2\alpha) e} \exp\left(-b_\alpha \left(\frac{r(s)}{R_h}\right)^{1/\alpha}\right),$$

where

$$r^2(s) = ((s_x - c_x) \cos(\vartheta) - (s_y - c_y) \sin(\vartheta))^2 + ((s_x - c_x) \sin(\vartheta) + (s_y - c_y) \cos(\vartheta))^2 / e^2.$$

The Sérsic profile specified above contains six parameters $(c, \lambda, \alpha, R_h, \vartheta, e)$ (see Table 1 for their interpretations). $r(s)$ is the ellipsoidal distance from $s = (s_x, s_y) \in \mathcal{S}$ to the known galactic center $c = (c_x, c_y)$ where the ellipsoidal coordinate is determined by the orientation angle ϑ and the aspect ratio e . We assume that ϑ and e are known, since these parameters of GC systems often align closely with those of the galactic light distribution and are measured with relatively high precision (Kissler-Patig et al. 1997; Gómez et al. 2001; Wang et al. 2013; Saifollahi et al. 2022).

We assume there are N_G ETGs and N_U UDGs in an image \mathcal{S} . The main type of ETG we encounter in our data are smaller elliptical galaxies in the Perseus cluster. We assume the GC point processes from all galaxies in image \mathcal{S} are independent. Thus,

$$\Lambda'_G(s) = \sum_{g=1}^{N_G} \text{Sérsic}(s; \lambda_g, R_h^g, \alpha_g),$$

$$\Lambda'_U(s) = \sum_{u=1}^{N_U} \text{Sérsic}(s; \lambda_u, R_h^u, \alpha_u),$$

and

$$\Lambda'(s) = \lambda_0 + \Lambda'_G(s) + \Lambda'_U(s). \quad (10)$$

The subscripts g and u in the above represent ETGs and UDGs/LSBGs respectively. We denote the index sets $\{1, \dots, n\}$ and $\{0, \dots, n\}$ by $[n]$ and $\langle n \rangle$, respectively, for any positive integer n . For simplicity, we reindex the intensity functions above with $k \in \langle N \rangle$ where $N = N_G + N_U$. Let $\Lambda'_0(s) = \lambda_0$ and $\Lambda'_k(s)$, $k \in [N]$ be the GC intensity for one of the galaxies, so

$$\Lambda'(s) = \sum_{k=0}^N \Lambda'_k(s).$$

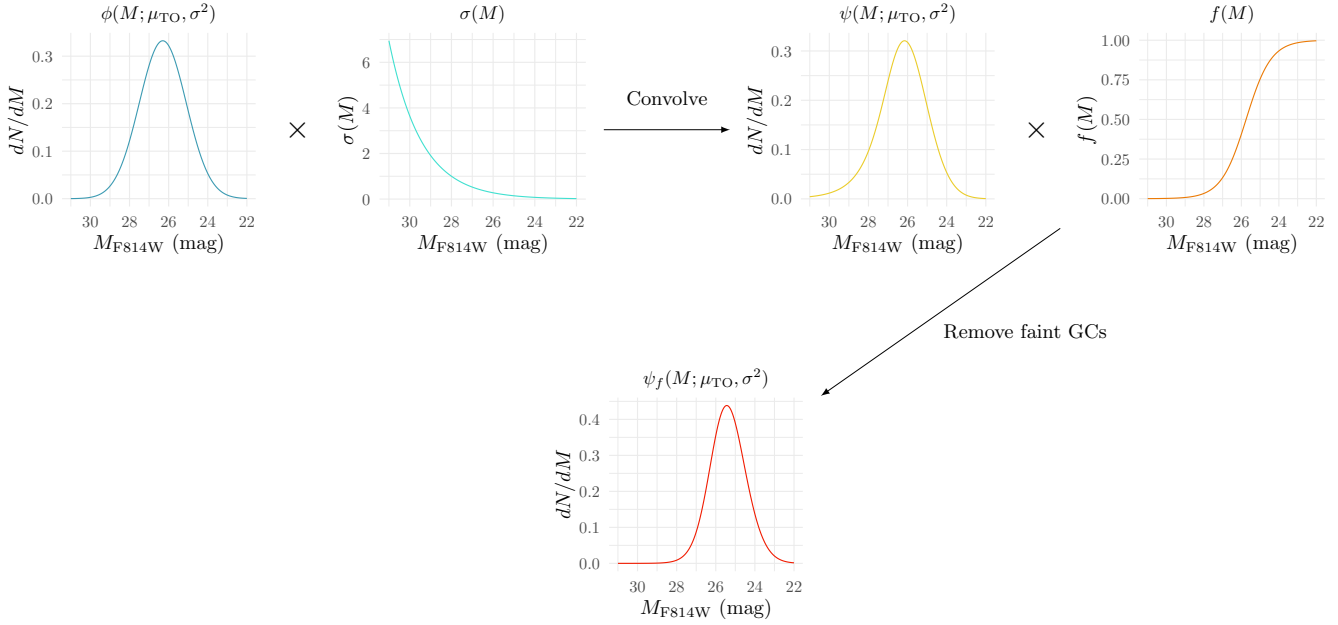


Figure 3. Illustration of our approach to obtain the observed GCLF from the true GCLF. The true GCLF ($\phi(\cdot; \mu_{\text{TO}}, \sigma^2)$; blue) is described by a Gaussian density $\phi(\cdot)$ with TO μ_{TO} and dispersion σ . It is then convolved with the magnitude uncertainty ($\sigma(M)$; turquoise) to obtain the noisy GCLF ($\psi(\cdot)$; yellow). The noisy GCLF is then truncated by the completeness fraction ($f(M)$; orange) to obtain the final observed GCLF ($\psi_f(\cdot)$; red).

Correspondingly, the intensity of the observed/thinned GC point process \mathbf{X} is

$$\Lambda(s) = \sum_{k=0}^N \Lambda_k(s),$$

where $\Lambda_k(s) = \Lambda'_k(s)\rho_k(s)$, and $\rho_k(s)$ follows from Eq. 6. The previous holds since the removal/thinning of faint GCs are independently applied to each of the $N + 1$ GC sub-population. Next, we introduce our modeling strategy for the GC magnitudes, and derive $\rho_k(s)$.

3.4.2. Modeling the Magnitudes (Mark)

Let n be the number of GCs observed in an image. We model the conditional distribution of the observed magnitude $\mathbf{M} = \{M_i\}_{i=1}^n$, given $\mathbf{X} = \{\mathbf{s}_i\}_{i=1}^n$ and Λ' , with a mixture distribution. Each mixture component models the observed GC magnitude distribution in each of the $N + 1$ sub-populations:

$$M_i \mid \mathbf{s}_i, \Lambda', \mu_{\text{TO}}^k, \sigma_k \sim \sum_{k=0}^N \pi_k(\mathbf{s}_i) \mathcal{N}_f(\mu_{\text{TO}}^k, \sigma_k^2). \quad (11)$$

The mixture probability that the i -th GC comes from the k -th sub-population is

$$\pi_k(\mathbf{s}_i) = \Lambda'_k(\mathbf{s}_i) / \Lambda'(\mathbf{s}_i). \quad (12)$$

We denote the observed GC magnitude distribution in the k -th sub-population by the random variable $\mathcal{N}_f(\mu_{\text{TO}}^k, \sigma_k^2)$, where μ_{TO}^k and σ_k are the mean and standard deviation of the true GCLF of the k -th sub-population. By Eq. 4, the p.d.f. of $\mathcal{N}_f(\mu_{\text{TO}}^k, \sigma_k^2)$ is:

$$\begin{aligned} \psi_f(m; \mu_{\text{TO}}^k, \sigma_k^2) &= \frac{\psi(m; \mu_{\text{TO}}^k, \sigma_k^2) f(m)}{\int_{-\infty}^{\infty} \psi(m; \mu_{\text{TO}}^k, \sigma_k^2) f(m) dm} \\ &\triangleq \frac{\psi(m; \mu_{\text{TO}}^k, \sigma_k^2) f(m)}{\Psi_f^k}, \end{aligned} \quad (13)$$

where $\psi(m; \mu_{\text{TO}}^k, \sigma_k^2)$ is the noisy GCLF (where the measurement uncertainties of the magnitudes are considered).

Figure 3 gives a visual representation of our approach to obtain the p.d.f. of $\mathcal{N}_f(\mu_{\text{TO}}^k, \sigma_k^2)$ from the true GCLF. Essentially, $\mathcal{N}_f(\mu_{\text{TO}}^k, \sigma_k^2)$ is the noisy magnitude distribution after thinning by the completeness fraction $f(m)$ (cf. Eq. 4).

The measured (noisy) magnitude M is generated through the following hierarchical model:

$$\begin{aligned} M \mid M_t &\sim \mathcal{N}(M_t, \sigma_M^2(M_t)), \\ M_t \mid \mu_{\text{TO}}^k, \sigma_k &\sim \mathcal{N}(\mu_{\text{TO}}^k, \sigma_k^2) \end{aligned} \quad (14)$$

where M_t is the true magnitude and $\sigma_M(\cdot)$ is the measurement uncertainty of the magnitude, as described in Section 2. The p.d.f. of M is thus

$$\psi(m; \mu_{\text{TO}}^k, \sigma_k^2) =$$

Parameter	Meaning	Unit	Prior	Hyper-parameters
$\log(\lambda_0)$	Log-intensity of \mathbf{X}'_{IGM}	kpc^{-2}	$\mathcal{N}(\log(\ell_0), \sigma_b^2)$	ℓ_0 varies [†] , $\sigma_b = 0.4$
λ_u	Mean number of GCs in UDGs	-	fold-Normal(μ_u, σ_u^2)	$\mu_u = 0, \sigma_u = 50$
$\log(R_h^u)$	Log-half-number radius of UDG GC systems	kpc	$\mathcal{N}(\log(R_e^u), \sigma_{r,u}^2)$	R_e^u varies [†] , $\sigma_{r,u} = 0.5$
$\log(\alpha_u)$	Log-Sérsic index of UDG GC systems	-	$\mathcal{N}(\log(\alpha_u^0), \sigma_{\alpha,u}^2)$	$\alpha_u^0 = 1, \sigma_{\alpha,u} = 0.75$
$\log(\lambda_g)$	Log-mean number of GCs in ETGs	-	$\mathcal{N}(\log(N_{\text{SF}}^g), \sigma_g^2)$	N_{SF}^g varies [†] , $\sigma_g = 0.25$
$\log(R_h^g)$	Log-half-number radius of ETG GC systems	kpc	$\mathcal{N}(\log(3.7R_e^g), \sigma_{r,g}^2)$	R_e^g varies [†] , $\sigma_{r,g} = 0.5$
$\log(\alpha_g)$	Log-Sérsic index of ETG GC systems	-	$\mathcal{N}(\log(\alpha_g^0), \sigma_{\alpha,g}^2)$	$\alpha_g^0 = 0.5, \sigma_{\alpha,g} = 0.5$
μ_{TO}	GCLF TO point	mag	$\mathcal{N}(\mu_0, \sigma_\mu^2)$	$\mu_0 = 26.3, \sigma_\mu = 0.5$
$\log(\sigma)$	Log-GCLF dispersion	mag	$\mathcal{N}(\log(\sigma_0), \tau_s^2)$	$\sigma_0 = 1.3, \tau_s = 0.25$

[†]See Appendix D

Table 2. Prior distributions for parameters in our model.

$$\int_{-\infty}^{\infty} \phi(m; m_t, \sigma_M^2(m_t)) \phi(m_t; \mu_{\text{TO}}^k, \sigma_k^2) dm_t,$$

where $\phi(m_t; \mu_{\text{TO}}^k, \sigma_k^2)$ is the true GCLF. The term $\phi(m; m_t, \sigma_M^2(m_t))$ is the uncertainty distribution for the observed magnitude m , which is also assumed to be Gaussian. Ψ_f^k is then the proportion of GCs that we can observe in the k -th sub-population. Computationally, we rely on numerical integration to obtain $\psi(m; \mu_{\text{TO}}^k, \sigma_k^2)$ and Ψ_f^k .

Combining everything from before, our complete hierarchical MATHPOP model is

$$\begin{aligned} \Lambda'_0(s) &= \lambda_0, \\ \Lambda'_k(s) &= \text{Sérsic}(s; \lambda_k, R_h^k, \alpha_k), k \geq 1 \\ M_i \mid \mathbf{s}_i, \Lambda', \mu_{\text{TO}}^k, \sigma_k &\sim \sum_{k=0}^N \pi_k(\mathbf{s}_i) \mathcal{N}_f(\mu_{\text{TO}}^k, \sigma_k^2), i \in [n] \\ \pi_k(s) &= \Lambda'_k(s) / \Lambda'(s), \\ \Lambda_k(s) &= \Lambda'_k(s) \Psi_f^k, \\ \Lambda(s) &= \sum_{k=0}^N \Lambda_k(s), \\ \mathbf{X} \mid \Lambda &\sim \text{IPP}(\Lambda). \end{aligned} \quad (15)$$

3.5. Prior Distributions and Posterior Sampling

The prior distributions for our model parameters are in Table 2. The explanation and motivation for choosing these priors are given in Appendix D.

To fit our MATHPOP model, we use a Markov chain Monte-Carlo (MCMC) algorithm to sample from the posterior distribution. Specifically, we construct an adaptive Metropolis algorithm (Haario et al. 2001; Roberts & Rosenthal 2009). The details of the algorithm are given in the Appendix E.

We run three independent Markov chains for each image. The chain length is catered to the complexity of the images — images with more galaxies have more iterations. Posterior convergence diagnostics such as potential scale reduction factors and effective sample size are computed and assessed using the R package `posterior` (Bürkner et al. 2023).

4. RESULTS

In this section, we present the results and analysis obtained by fitting our MATHPOP model to the GC data obtained from the PIPER survey.

4.1. GC Counts

Figure 4 compares our MATHPOP model estimates of the number of GCs ($N_{\text{GC}}^{\text{est}}$) to the number of GCs estimated by the standard approach (N_{NG}) using the binary GC catalog from J24 (hereafter Binary J24 catalog). The orange circles and the red triangles are the posterior mean and mode from our MATHPOP results, respectively. The widths of the blue boxes show the uncertainty in our estimates (68% credible interval) and the heights show the uncertainty in the J24 estimates (two standard errors). The left panel of Figure 4 presents the MATHPOP results based on the probabilistic GC catalog from the DOLPHOT point sources (hereafter L24 catalog), and the right panel shows the results obtained from the probabilistic GC catalog obtained using the point source list from J24 (hereafter Prob J24 catalog).

For LSBGs with higher estimates of N_{GC} , our credible intervals are wider than those from the standard approach. The reverse is true for LSBGs with low GC counts. This is expected since the variance of the Poisson distribution increases with the mean. Furthermore, MATHPOP fully accounts for all sources of uncertainties. In contrast, the standard approach assumes that μ_{TO}

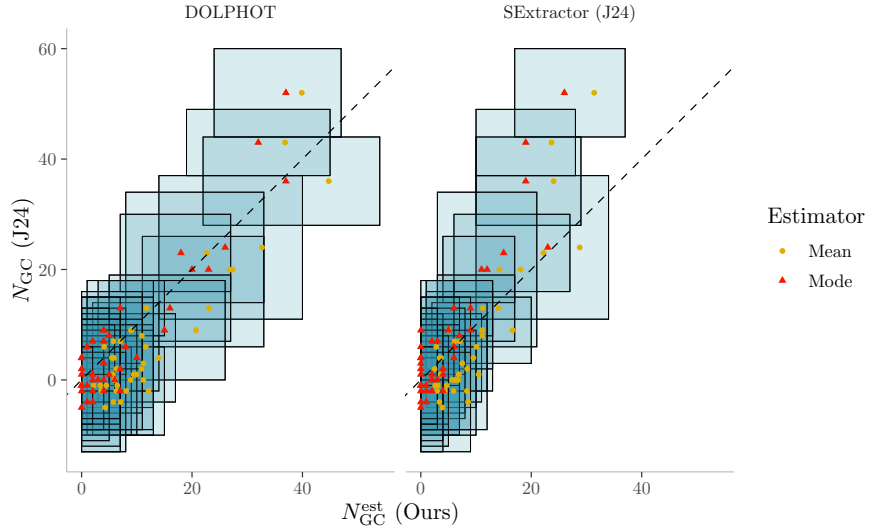


Figure 4. Comparison of the estimated number of GCs around LSBGs. Left: results ($N_{\text{GC}}^{\text{est}}$) obtained from MATHPOP using the L24 catalog (using point sources from DOLPHOT) vs. the standard approach ($N_{\text{GC}}(\text{J24})$). Right: results ($N_{\text{GC}}^{\text{est}}$) obtained from MATHPOP using the Prob J24 catalog (J24 point source data, SExtractor) vs. the standard approach ($N_{\text{GC}}(\text{J24})$). Red triangles are our posterior mode estimates, yellow points are our posterior mean estimates. The blue boxes are the uncertainties of each estimate: the height of the box is $2\times$ the standard error of the estimates from the standard approach; width of the box is the 68% credible intervals from our estimates. Black dashed lines are the $y = x$ reference line.

is fixed and does not account for its uncertainty. For LSBGs with low N_{GC} , our uncertainty ranges are lower bounded by zero, so our credible intervals are much narrower than those from the standard approach.

Based on the left panel of Figure 4 and taking into account the statistical uncertainty, MATHPOP results and those from the standard approach generally agree. At first glance, it seems that the posterior mode is a better summary statistic than the posterior mean, especially for LSBGs with lower N_{GC} . This is expected since the posterior distributions of Poisson counts are generally right skewed, and the skewness is even more pronounced for low-count Poisson distributions. For a detailed account on which summary statistic is the best for N_{GC} , we assess the performance of different estimators through simulations in Section 4.4.1. In short, for low- N_{GC} LSBGs, we strongly recommend using the posterior mode as the point estimate due to the aforementioned skewness of the posterior distribution.

The right panel of Figure 4 shows that the results obtained from MATHPOP using the Prob J24 catalog are typically lower than MATHPOP estimates using L24 catalog and those from the standard approach.

An advantage of MATHPOP is that, for low- N_{GC} LSBGs, the estimates and credible intervals do not extend below zero. Moreover, MATHPOP provides the poste-

rior probability that an LSBG does not have any GCs ($\mathbb{P}(N_{\text{GC}} = 0)$, Table 3). As seen in Table 3, the MATHPOP results show that LSBGs with $\mathbb{P}(N_{\text{GC}} = 0) > 5\%$ generally have N_{GC} estimates significantly above zero, and vice versa. Simulations are carried out in later sections to study how $\mathbb{P}(N_{\text{GC}} = 0)$ behaves.

The detailed posterior summary statistics of GC system properties obtained using L24 catalog, as well as N_{GC} estimates quoted from the standard approach, are given in Table 3. The results obtained using Prob J24 catalog are not shown in Table 3 due to space constraints. We stress that the point estimates in Table 3 should only be used as a rough guide, as different types of point estimators under Bayesian approach optimize different statistical properties. It is up to the reader to decide which of these properties are preferred. Best practice is to treat the parameters as random variables and to consider their estimated value and uncertainty based on the entire posterior distribution.

Despite the good alignment of estimates from MATHPOP and those from the standard approach, the results from Table 3 indicate that for R27 and R84, although not statistically significant, our point estimates of N_{GC} are much lower than those from the standard approach. We will investigate this discrepancy in the next section.

4.2. R27 and R84: A Diagnostic

ID	α	δ	$N_{\text{GC}}^{\text{est}}$	$N_{\text{GC}}^{\text{est}}$	N_{GC} (J24)	$\mathbb{P}(N_{\text{GC}} = 0)$	μ_{TO}	σ	R_h	UDG?
	(J2000.0)	(J2000.0)	Mode	Mean			(mag)	(mag)	(kpc)	
R21	03:20:29.5	41:44:51.0	37_{-15}^{+17}	44.76	36 ± 8	0.000	$26.13_{-0.36}^{+0.39}$	$1.21_{-0.26}^{+0.19}$	$2.35_{-0.65}^{+0.87}$	✓
R27	03:19:43.6	41:42:46.8	37_{-13}^{+10}	39.88	52 ± 8	0.000	$25.75_{-0.24}^{+0.32}$	$0.99_{-0.26}^{+0.14}$	$2.03_{-0.52}^{+0.65}$	✗
R84	03:17:24.9	41:44:21.5	32_{-13}^{+13}	36.85	43 ± 6	0.000	$26.12_{-0.39}^{+0.42}$	$1.28_{-0.28}^{+0.19}$	$1.33_{-0.32}^{+0.41}$	✓
W88	03:19:59.1	41:18:32.4	26_{-12}^{+14}	32.67	24 ± 13	0.000	$25.82_{-0.26}^{+0.43}$	$1.30_{-0.33}^{+0.23}$	$3.80_{-1.16}^{+1.65}$	✓
R60	03:19:36.2	41:57:26.2	23_{-12}^{+10}	27.34	20 ± 6	0.000	$26.01_{-0.43}^{+0.48}$	$1.28_{-0.32}^{+0.22}$	$1.05_{-0.34}^{+0.47}$	✗
W89	03:20:00.1	41:17:05.4	20_{-12}^{+13}	26.80	17 ± 14	0.000	$26.29_{-0.38}^{+0.43}$	$1.12_{-0.32}^{+0.21}$	$1.53_{-0.60}^{+0.77}$	✓
R16	03:18:36.5	41:11:32.1	18_{-11}^{+9}	22.66	23 ± 7	0.000	$26.11_{-0.38}^{+0.44}$	$1.14_{-0.33}^{+0.20}$	$3.81_{-1.27}^{+1.77}$	✓
R5	03:17:34.6	41:45:21.6	16_{-11}^{+11}	23.07	13 ± 6	0.000	$26.29_{-0.48}^{+0.45}$	$1.38_{-0.34}^{+0.21}$	$1.12_{-0.61}^{+0.88}$	✓
W29	03:18:23.3	41:45:00.6	15_{-10}^{+11}	20.73	9 ± 9	0.003	$26.44_{-0.46}^{+0.42}$	$1.23_{-0.32}^{+0.21}$	$1.85_{-0.66}^{+0.75}$	✗
W56	03:18:48.1	41:14:02.2	10_{-7}^{+7}	13.94	4 ± 8	0.003	$26.22_{-0.46}^{+0.46}$	$1.18_{-0.32}^{+0.21}$	$0.48_{-0.19}^{+0.33}$	✗
W79	03:18:21.2	41:46:15.3	8_{-6}^{+6}	11.63	6 ± 8	0.007	$26.27_{-0.44}^{+0.46}$	$1.16_{-0.35}^{+0.20}$	$1.23_{-0.55}^{+0.89}$	✓
R15	03:17:03.8	41:14:55.0	7_{-4}^{+8}	11.76	13 ± 5	0.008	$26.48_{-0.41}^{+0.48}$	$1.08_{-0.34}^{+0.21}$	$1.87_{-0.74}^{+1.10}$	✓
W22	03:18:05.4	41:27:42.1	7_{-5}^{+8}	12.12	-2 ± 8	0.013	$26.33_{-0.47}^{+0.45}$	$1.21_{-0.35}^{+0.20}$	$1.39_{-0.52}^{+0.67}$	✗
W12	03:17:36.7	41:23:00.9	7_{-6}^{+6}	10.86	2 ± 7	0.012	$26.36_{-0.44}^{+0.45}$	$1.16_{-0.35}^{+0.20}$	$1.33_{-0.62}^{+0.82}$	✓
W7 (V12)	03:17:16.0	41:20:11.7	6_{-5}^{+7}	11.18	0 ± 10	0.017	$26.50_{-0.46}^{+0.45}$	$1.11_{-0.34}^{+0.20}$	$0.95_{-0.39}^{+0.45}$	✗
W1	03:17:00.4	41:19:20.6	5_{-4}^{+8}	10.90	8 ± 10	0.020	$26.26_{-0.50}^{+0.48}$	$1.26_{-0.39}^{+0.25}$	$1.39_{-0.66}^{+1.09}$	✓
W13	03:17:38.2	41:31:56.6	5_{-5}^{+6}	9.44	1 ± 7	0.022	$26.27_{-0.53}^{+0.46}$	$1.35_{-0.36}^{+0.23}$	$1.03_{-0.44}^{+0.59}$	✗
W5	03:17:10.9	41:34:03.6	4_{-4}^{+7}	9.01	9 ± 7	0.036	$26.38_{-0.45}^{+0.47}$	$1.11_{-0.36}^{+0.22}$	$1.96_{-0.97}^{+1.46}$	✓
W7 (V14)	03:17:16.0	41:20:11.7	4_{-4}^{+10}	8.88	0 ± 10	0.038	$26.34_{-0.50}^{+0.47}$	$0.92_{-0.62}^{+0.23}$	$0.94_{-0.42}^{+0.57}$	✗
W17	03:17:44.1	41:21:18.7	4_{-4}^{+4}	7.00	7 ± 6	0.032	$26.23_{-0.47}^{+0.49}$	$1.22_{-0.37}^{+0.23}$	$0.99_{-0.43}^{+0.69}$	✓
R23	03:19:51.5	41:54:35.6	4_{-3}^{+7}	8.98	9 ± 6	0.031	$26.37_{-0.50}^{+0.48}$	$1.21_{-0.39}^{+0.23}$	$2.14_{-1.02}^{+1.82}$	✓
R20	03:20:24.6	41:43:28.6	4_{-4}^{+5}	8.08	-2 ± 8	0.039	$26.17_{-0.52}^{+0.52}$	$1.37_{-0.39}^{+0.25}$	$0.99_{-0.47}^{+0.75}$	✓
W4	03:17:07.1	41:22:52.4	4_{-4}^{+9}	11.21	3 ± 12	0.044	$26.32_{-0.46}^{+0.52}$	$0.95_{-0.61}^{+0.24}$	$3.28_{-1.44}^{+2.08}$	✗
W8	03:17:19.6	41:34:32.0	3_{-3}^{+4}	6.02	0 ± 7	0.071	$26.44_{-0.50}^{+0.46}$	$1.15_{-0.39}^{+0.22}$	$1.08_{-0.48}^{+0.77}$	✓
W80	03:19:39.2	41:13:43.5	2_{-2}^{+5}	5.76	7 ± 8	0.078	$26.41_{-0.48}^{+0.50}$	$1.18_{-0.36}^{+0.24}$	$1.30_{-0.61}^{+0.76}$	✗
W6	03:17:13.3	41:22:07.5	2_{-2}^{+5}	6.29	-2 ± 10	0.080	$26.33_{-0.50}^{+0.52}$	$1.15_{-0.73}^{+0.28}$	$0.62_{-0.31}^{+0.45}$	✗
W59	03:18:54.3	41:15:28.9	2_{-2}^{+5}	5.92	0 ± 9	0.082	$26.30_{-0.52}^{+0.50}$	$1.27_{-0.38}^{+0.23}$	$0.60_{-0.29}^{+0.42}$	✗
W2	03:17:03.3	41:20:28.7	0_{-0}^{+11}	9.93	1 ± 10	0.082	$26.40_{-0.50}^{+0.49}$	$1.19_{-0.37}^{+0.23}$	$3.74_{-1.76}^{+2.46}$	✗
W18	03:17:48.4	41:18:39.3	2_{-2}^{+6}	7.07	-4 ± 9	0.083	$26.36_{-0.53}^{+0.48}$	$1.22_{-0.39}^{+0.23}$	$2.13_{-1.05}^{+2.03}$	✓
W14	03:17:39.2	41:31:03.5	1_{-1}^{+7}	6.46	-1 ± 7	0.089	$26.40_{-0.50}^{+0.50}$	$1.21_{-0.39}^{+0.21}$	$1.04_{-0.50}^{+0.78}$	✗
R117	03:18:03.8	41:27:08.8	2_{-2}^{+5}	5.65	1 ± 8	0.094	$26.30_{-0.49}^{+0.52}$	$1.31_{-0.39}^{+0.22}$	$0.65_{-0.31}^{+0.46}$	✗
R79	03:18:21.2	41:46:15.3	1_{-1}^{+7}	5.74	-4 ± 9	0.102	$26.38_{-0.52}^{+0.50}$	$1.22_{-0.39}^{+0.22}$	$0.95_{-0.46}^{+0.66}$	✗
R116	03:17:46.0	41:30:11.6	0_{-0}^{+7}	5.85	4 ± 8	0.130	$26.50_{-0.52}^{+0.49}$	$1.18_{-0.39}^{+0.22}$	$1.22_{-0.54}^{+0.88}$	✗
W28	03:18:21.7	41:45:27.5	0_{-0}^{+7}	6.30	2 ± 9	0.132	$26.48_{-0.51}^{+0.51}$	$1.17_{-0.38}^{+0.23}$	$0.65_{-0.35}^{+0.50}$	✗
W83	03:19:47.4	41:44:08.8	1_{-1}^{+5}	4.07	6 ± 7	0.134	$26.37_{-0.48}^{+0.50}$	$1.20_{-0.37}^{+0.24}$	$0.67_{-0.30}^{+0.47}$	✗
W25	03:18:15.5	41:28:35.3	0_{-0}^{+6}	5.49	4 ± 6	0.167	$26.41_{-0.53}^{+0.50}$	$1.25_{-0.40}^{+0.23}$	$1.09_{-0.54}^{+0.82}$	✗
R14	03:17:06.1	41:13:03.2	0_{-0}^{+5}	4.48	-1 ± 5	0.178	$26.47_{-0.55}^{+0.52}$	$1.18_{-0.39}^{+0.22}$	$1.39_{-0.73}^{+1.15}$	✓
W19	03:17:53.1	41:19:31.9	0_{-0}^{+5}	4.27	-5 ± 6	0.195	$26.46_{-0.52}^{+0.54}$	$1.21_{-0.41}^{+0.24}$	$1.94_{-0.93}^{+1.37}$	✓
W16	03:17:41.8	41:24:02.0	0_{-0}^{+4}	3.54	-2 ± 7	0.217	$26.42_{-0.52}^{+0.49}$	$1.21_{-0.39}^{+0.24}$	$1.21_{-0.60}^{+0.78}$	✗
R89	03:20:12.8	41:44:57.7	0_{-0}^{+4}	3.38	-1 ± 7	0.261	$26.46_{-0.54}^{+0.52}$	$1.21_{-0.41}^{+0.23}$	$0.53_{-0.26}^{+0.37}$	✗
W84	03:19:49.7	41:43:42.4	0_{-0}^{+2}	2.16	-1 ± 7	0.335	$26.40_{-0.50}^{+0.54}$	$1.22_{-0.39}^{+0.25}$	$0.68_{-0.34}^{+0.45}$	✗

Table 3. Posterior predictive summary of GC system properties of 40 LSBGs in the PIPER survey. α and δ are the celestial coordinates of the LSBGs in right ascension and declination, respectively. The posterior mode of N_{GC} together with the 68%-highest posterior density interval is given in column 4. Posterior mean of N_{GC} are given in columns 5. Column 6 contains the N_{GC} estimates from J24. $\mathbb{P}(N_{\text{GC}} = 0)$ is the probability that an LSBG has no GCs. μ_{TO} and σ give the posterior mode of the GCLF TO points and dispersion, respectively. R_h is the posterior mode of the half-number radius of GC systems. The last column indicates whether or not an LSBG meets the strict criteria of being a UDG. The horizontal line separates the LSBGs into ones with $\mathbb{P}(N_{\text{GC}} = 0) \leq 0.05$ (above horizontal line), and ones with $\mathbb{P}(N_{\text{GC}} = 0) > 0.05$ (below horizontal line).

We investigate the difference in the results from different data and approaches by analyzing R27 and R84 in more detail. Figure 5 shows the spatial locations of the GC candidates from the three GC catalogs around R27 and R84 within a circular diameter of 15 kpc, which is the aperture size used by the standard approach to derive N_{GC} estimates. The GCs are color-coded with their magnitudes in F814W. From left to right panels, the GC candidates, respectively, come from L24 catalog (DOLPHOT sources, left), Binary J24 catalog (SExtractor sources, binary classification, middle), and Prob J24 catalog (SExtractor sources, probabilistic classification, right). The size of the point is proportional to their probability of being a GC ($p(\text{GC})$). For Binary J24 catalog, points have a size of one as they are all fully considered as GCs. For visualization purposes, only points with $p(\text{GC}) > 0.05$ and redder than 0.8 mag are shown.

4.2.1. R27

In the top panel of Figure 5, the Binary J24 catalog has 37 GC candidates around R27 in the cutout, while L24 catalog has $\sim 27^2$ after adjusting for $p(\text{GC})$. After a simple correction of background contaminants in both catalogs (following the same procedure in J24), the numbers of GC candidates (~ 24) that can contribute to the final N_{GC} estimate in R27 are the same in both catalogs.

The main reason MATHPOP point estimate (37) is much lower than the standard approach (52) for R27 is the treatment of the GCLF. The standard approach assumes a fixed canonical GCLF TO of $\mu_{\text{TO}} = 26.3$ mag, while the posterior mode of the GCLF TO based on MATHPOP is half a magnitude brighter than the canonical μ_{TO} . A simple calculation shows that such a difference in μ_{TO} leads to $\sim 20\%$ reduction in the final N_{GC} estimate. Thus, if the GCLF is inferred using the Binary J24 catalog, the point estimate of N_{GC} in R27 will be reduced to ~ 42 . As a side note, W88 also has a much brighter inferred μ_{TO} (Table 3) than the canonical μ_{TO} , but MATHPOP estimate is almost the same as that from the standard approach. This is because the image (V11ACS) in which W88 resides is severely affected by background contaminants. In fact, numerous clear imaging artifacts and extended sources are seen in V11ACS from the Binary J24 catalog, which likely resulted in an overestimated background contaminant count under the standard approach and a similar N_{GC} estimate for W88.

Another minor reason that can further decrease N_{GC} estimate is the GC membership uncertainty. The stan-

dard approach assumes that all GC candidates within the 15 kpc aperture belong to R27, after accounting for background contaminants. However, simple corrections for background contaminants do not consider the spatial distribution of GCs. It is entirely possible that the GC candidates in the outer region of R27 shown in Figure 5 actually belong to the IGM. In fact, the average posterior probabilities ($\pi_k(s_i)$, cf. Eq. 12) that these outer region GC candidates do belong to R27 are only around 40 – 60%. Such high uncertainties further drives down the final point estimate of N_{GC} . We need to note that the GC membership uncertainty computed by MATHPOP is only the best estimate purely based on the spatial distribution of GCs and the Sérsic profile assumption. True GC membership will not be known without spectroscopy data.

4.2.2. R84

For R84, as seen in the bottom panel of Figure 5, the inferred μ_{TO} from our data is close to the canonical μ_{TO} , but the number of sources from L24 catalog is fewer. This is in part due to the point source selection criteria between DOLPHOT (L24) and SExtractor (J24).

Close inspection of the GC candidates around R84 that are in Binary J24 catalog but not in L24 catalog reveals that all are at the boundary of being point sources and extended sources to the human eye, and a few of them are also relatively red. Thus, the true nature of these sources is rather uncertain, and it is difficult to determine whether they are bona-fide GCs or background galaxies. Therefore, the difference in the number of GC candidates considered results in a rather large difference between MATHPOP point estimate and that from the standard approach.

4.2.3. Prob J24 Catalog

From the right panels of Figure 5, it is clear why the results obtained by using Prob J24 catalog are significantly lower than the other two: fainter sources have lower probability of being GCs within the Prob J24 catalog. This is caused by the significant contaminant population at the faint levels in the J24 point source list, which effectively reduces our ability to separate GCs from contaminants. The reduction of our discriminatory ability of faint sources then leads to a double whammy: sources that are true GCs at faint levels have lower impact in the model, which reduces the count estimates and also causes the inferred μ_{TO} to be much brighter. The brighter inferred μ_{TO} then further drives the final N_{GC} estimate downward.

Based on the analysis in Figure 5, the true N_{GC} for R27 and R84 should be upper bounded by estimates from the standard approach and lower bounded by the

² Computed by summing $p(\text{GC})$ for all sources.

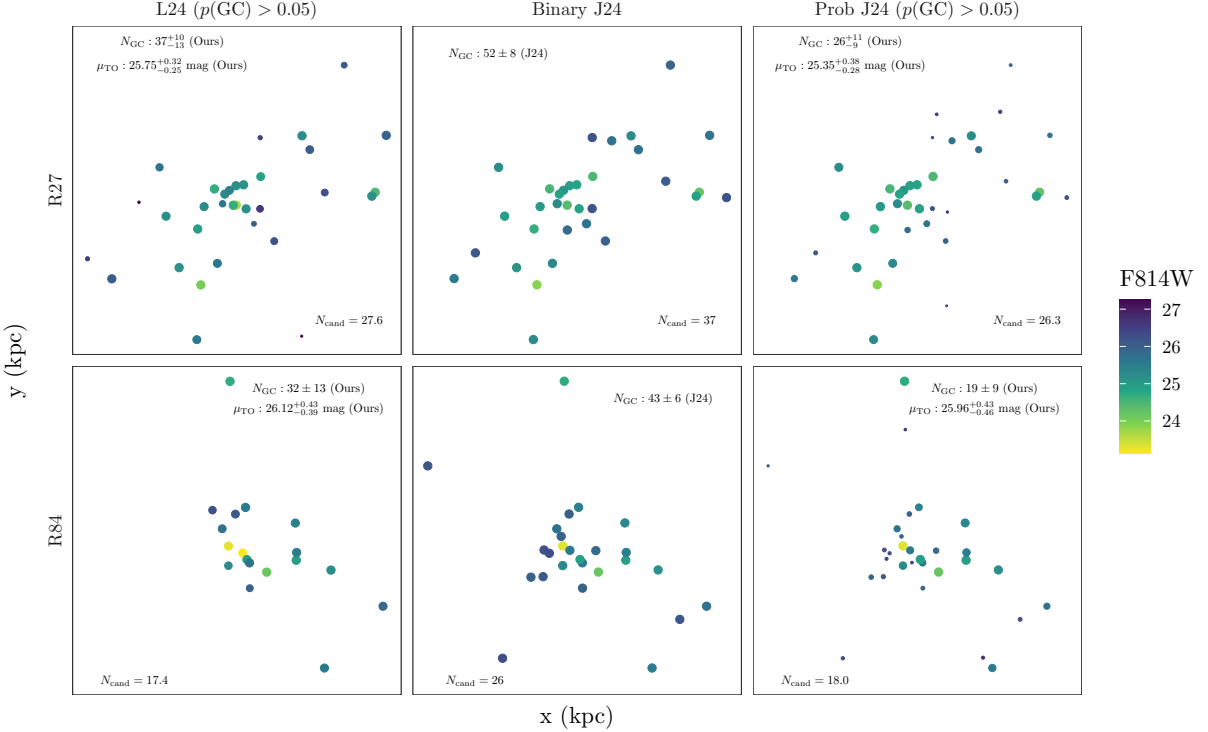


Figure 5. Spatial distribution of GC candidates around the LSBGs (top) R27 and (bottom) R84 within a 15 kpc diameter. For both top and bottom panels: colors are the magnitude of sources in F814W; left panels: GC candidates from L24 catalog; middle panels: GC candidates from Binary J24 catalog; right panels: GC candidates from Prob J24 catalog. The size of points in all panels are proportional to the probability that a source is a GC. For Binary J24 catalog, the size of the point is set to one as a reference, since they are all considered GCs. Estimates of N_{GC} based on each of the three catalogs are provided for both LSBGs. For L24 catalog and the Prob J24 catalog, the estimated (posterior mode) GCLF TO points (μ_{TO}) for the two galaxies are also provided. The numbers of GC candidates (N_{cand} ; not background-corrected) within the cutouts from each catalog are provided at the bottom of each sub-panel.

results from Prob J24 catalog. The results obtained using L24 catalog may be closest to the true value, since our point source catalog (L24) is carefully pruned and cleaned to ensure that the least number of contaminants are present. Furthermore, MATHPOP fully addresses all sources of uncertainties, such as inferring μ_{TO} from the data and the GC membership uncertainty.

As a final note, the construction of point source and GC catalogs has immense impact on the final results. Therefore, we recommend the use of ‘DOLPHOT+MATHPOP’ for GC catalog construction and inferring the GC counts. Point sources catalogs based on SExtractor, as seen previously, can contain so many contaminants that it is unlikely to produce reliable GC count estimates.

4.3. GCLF

From Table 3, the inferred μ_{TO} for most LSBGs considered here are close to the canonical $\mu_{\text{TO}} = 26.3$ mag. However, the results of R27 and W88 in Table 3 indicate that they have GCLFs weighted more toward the luminous end, with posterior mode estimates of μ_{TO} being more than half a magnitude brighter than the canonical value for both LSBGs. We computed the Bayes’ factor (BF; Kass & Raftery 1995) to determine the amount of evidence on whether μ_{TO} is indeed brighter than the canonical value for the two LSBGs using the Savage-Dickey method (bayestestR; Makowski et al. 2019, BF > 1 means there is evidence supporting the claim that μ_{TO} is brighter than the canonical value). The resulting BF values are 4.5 and 2.5 for R27 and W88, respectively.

In addition, as a post-hoc check and crude estimate, we use the GC candidates within 6 kpc of either LSBG from the L24 catalog, and apply a simple background-correction as in J24 to conduct maximum likelihood estimations (MLE) for R27 and W88 of their respective μ_{TO} with completeness fraction considered.

The fitted MLEs of μ_{TO} for R27 and W88 are $\mu_{\text{TO}}^{\text{R27}} = 25.42 \pm 0.17$ mag, $\sigma^{\text{R27}} = 0.72 \pm 0.12$ mag and $\mu_{\text{TO}}^{\text{W88}} = 25.17 \pm 0.31$ mag, $\sigma^{\text{W88}} = 0.83 \pm 0.21$ mag. The GCLF TO points for the two LSBGs are respectively ~ 0.9 mag and ~ 1.1 mag brighter than the canonical μ_{TO} of

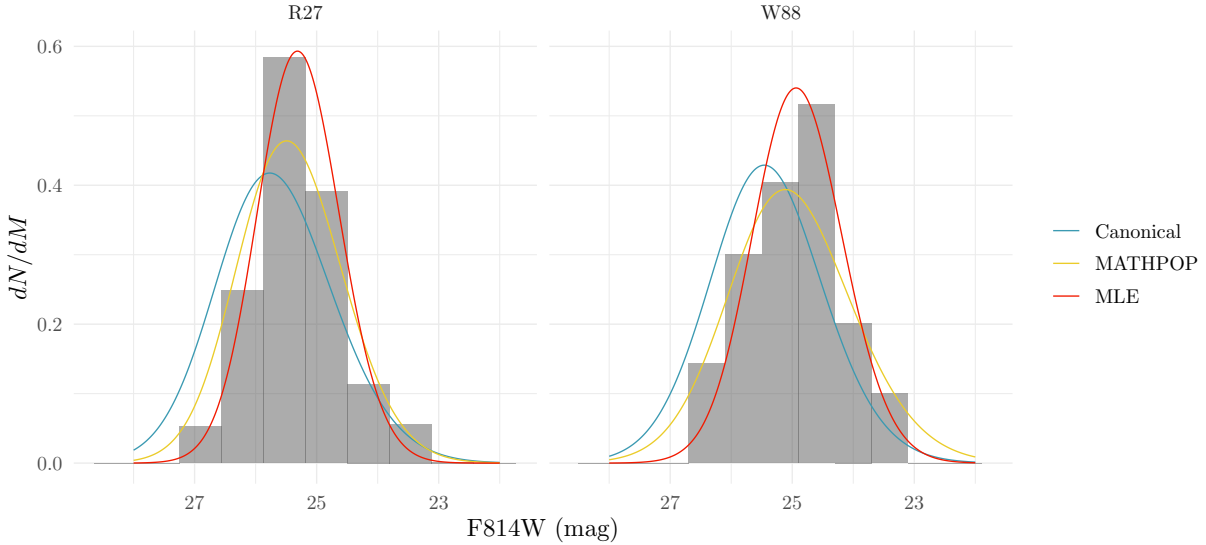


Figure 6. Observed GCLFs ($\psi_f(m; \mu_{\text{TO}}, \sigma^2)$) obtained from different approaches against the observed background-corrected GC magnitude data for R27 and W88. Colored lines are the observed GCLFs based on different assumptions/models. Histograms are the magnitudes of observed GC candidates within 6 kpc of the galactic center of each galaxy from the L24 catalog. For visualization purposes, uncertainties of estimates are omitted.

26.3 mag. The GCLF dispersions are also much smaller than the canonical value of 1 – 1.2 mag. The p -values under the null hypothesis that their μ_{TO} is equal to the canonical one are $\sim 10^{-8}$ and $\sim 10^{-5}$, respectively. Based on both the BF values and the MLE results, we thus have significant evidence that these two LSBGs have GCLFs that are significantly more weighted toward the luminous end.

Figure 6 shows the observed GCLFs for R27 and W88 from different approaches against the magnitude distributions of GC candidates within 6 kpc from the galactic center of both LSBGs. The histograms of GC magnitudes are obtained by resampling the magnitudes of sources (background-corrected) within 6 kpc from the galactic center of both LSBGs for 500 times according to the GC candidate probabilities from L24 catalog. For better visualization, uncertainties of estimates are omitted in the figure. The observed GCLFs are computed based on Eq. 13, where the values of μ_{TO} and σ are set to the posterior mode from MATHPOP, the previously obtained MLE, or the canonical value ($\mu_{\text{TO}} = 26.3$ mag, $\sigma = 1.2$ mag). It is clear that for R27 and W88, the canonical GCLF does not fit well to the observed data at all. The GCLFs obtained from the MLE approach closely align with the data as expected. The results from MATHPOP are in between the other two as the results from the Bayesian approach are a combination of information from the data and the prior distributions, with the latter based on the canonical values.

The observed top-heavy GCLFs of R27 and W88 put them in a similar category to NGC 1052 DF2 and DF4 (Shen et al. 2021). DF2 and DF4 have a double-peaked GCLF where there is a major peak that is ~ 1.5 mag brighter than the canonical TO point and a minor peak at the canonical TO point. However, it is unclear whether R27 and W88 are indeed of the same population and having similar formation scenario as DF2 and DF4, since DF2 and DF4 are much closer and the photometry is much more complete.

4.4. Simulated Data

In this section, we conduct a simulation analysis for our proposed model. Due to computational constraints, we simulate only the point patterns of GCs instead of other possible type of point sources such as foreground stars or background galaxies. Thus, every simulated source is considered a true GC, so the simulation results directly indicate the performance of our proposed model.

For simplicity, we only vary N_{GC} and μ_{TO} of a simulated UDG GC system. We consider an observation window of $76 \times 76 \text{ kpc}^2$ — the same as the field of view of ACS images in the PIPER survey. We first simulate the IGM GC locations using an HPP. N_{GC} from IGM is based on the IGM GC intensity estimated from V10WFC3. We then simulate the UDG GC system from a Sérsic profile and randomly place it in the field. The GC system has half-number radius $R_h = 2$ kpc, Sérsic index $\alpha = 2$, aspect ratio $e = 1$ and orientation angle $\vartheta = \pi/4$. N_{GC} takes a value in $\{0, 5, 10, 20, 40, 80\}$.

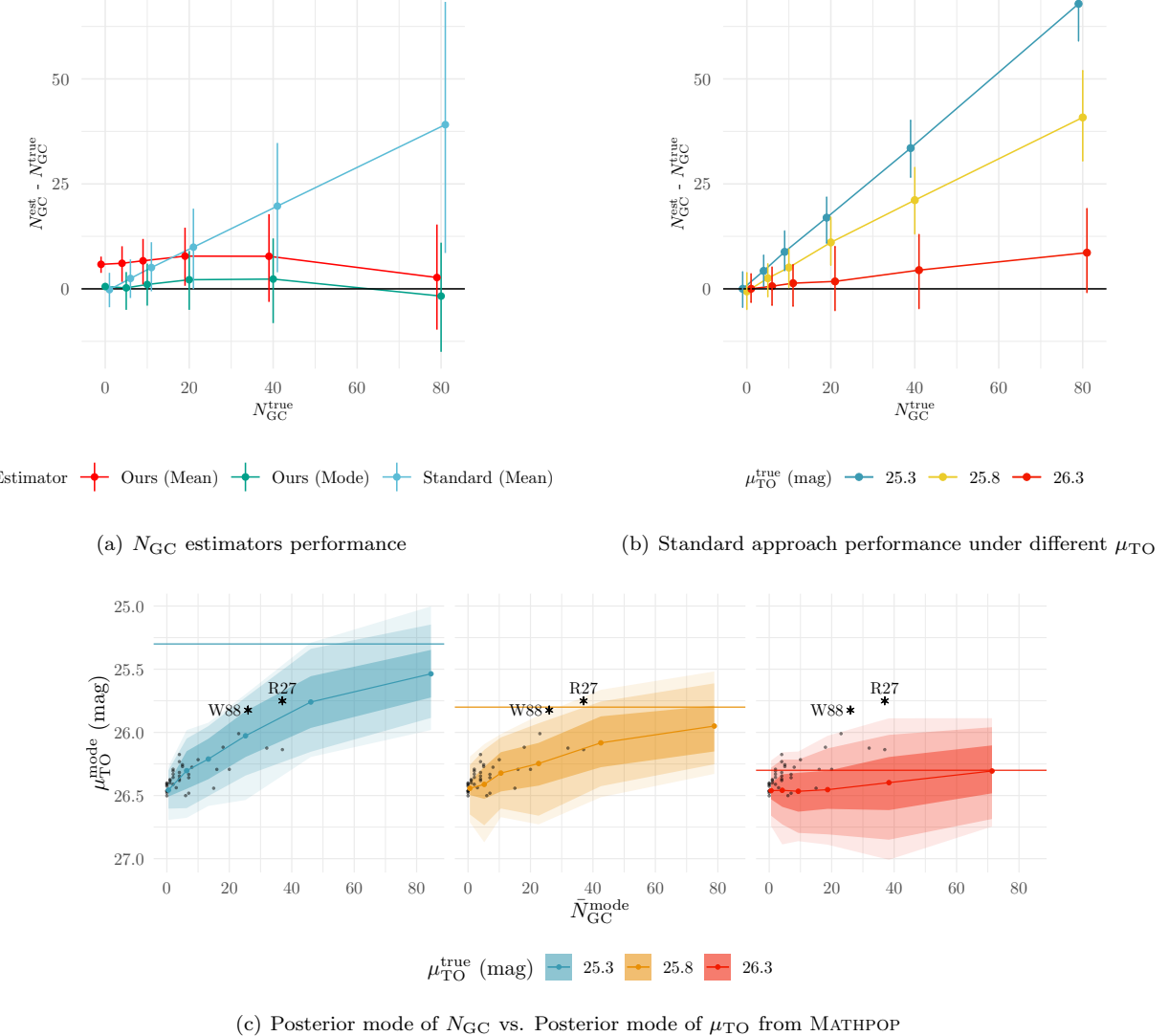


Figure 7. Results from simulation: (a) Point estimates performance (difference between estimates ($N_{\text{GC}}^{\text{est}}$) and true values ($N_{\text{GC}}^{\text{true}}$)) based on 450 simulated data for each $N_{\text{GC}}^{\text{true}}$; color represents different estimators. (b) Point estimates performance for $N_{\text{GC}}^{\text{true}}$ from the standard approach for different values of $\mu_{\text{TO}}^{\text{true}}$; color represents $\mu_{\text{TO}}^{\text{true}}$. In both (a) and (b), error bars are the central 68% quantile intervals based on the simulations; a trend that is flat and close to $y = 0$ line indicates better performance. (c) Average posterior mode estimates of the GC counts ($\bar{N}_{\text{GC}}^{\text{mode}}$) vs. posterior mode of the GCLF TO ($\mu_{\text{TO}}^{\text{mode}}$). The colored points are the respective average posterior mode estimates while the error bands (with decreasing transparency) are the 68, 95, and 99% central quantile bands for $\mu_{\text{TO}}^{\text{mode}}$. The horizontal lines represent the true values of μ_{TO} we used to simulate the GCLF for our UDG. The gray points are the posterior mode estimates of all the LSBGs obtained using L24 catalog. W88 and R27 are marked by black stars.

After the GC point pattern is obtained, we simulate a magnitude for each GC. For GCs in the IGM, they have a canonical GCLF with $\mu_{\text{TO}} = 26.3$ mag and dispersion of 1.2 mag. For GCs in the UDG, they have a GCLF with $\mu_{\text{TO}} = \{25.3, 25.8, 26.3\}$ mag and dispersion of 1.0 mag. We then jitter these “true” magnitudes with simulated measurement uncertainties and remove faint GCs using the completeness fraction based on the AST results using DOLPHOT for ACS images. Our model is then fitted to the resulting simulated GC point pattern

and magnitude data. For comparison, we also apply the standard approach to the simulated data. Under the standard approach, the simulated data have measurement uncertainties, the completeness fraction follows that from J24, and GCs fainter than 26.3 mag are removed.

We repeat the above process 150 times for each parameter configuration, resulting in a total of $6 \times 3 \times 150 = 2700$ different simulated data. The results are provided and analyzed below.

4.4.1. GC counts

Figure 7(a) shows the performance of N_{GC} estimates from MATHPOP and the standard approach based on the simulated data. On average, the posterior modes from our model nicely match the true N_{GC} . Additionally, the posterior mode is a much better point estimate for N_{GC} than the posterior mean. As mentioned, this is due to the highly right-skewed nature of the posterior distribution of N_{GC} . For UDGs with low N_{GC} , the posterior mean, as a point estimator, completely overestimates N_{GC} . Therefore, Figure 7(a) is a definitive showcase that the posterior mode should be used as a point estimator for N_{GC} .

On the other hand, Figure 7(a) also demonstrates that the standard approach severely overestimates N_{GC} , which is caused by the assumption on GCLF. As seen in Figure 7(b), the standard approach is only accurate when the true μ_{TO} is the canonical value of 26.3 mag, while for brighter μ_{TO} , the standard approach produces completely inaccurate estimates. Since the standard approach assumes all UDGs have the canonical GCLF, the final N_{GC} estimates are overestimates if the true μ_{TO} is brighter than the canonical one.

On another note, we have also tested the effect of the GC system size under the standard approach. We found the assumption that a counting aperture with diameter of 15 kpc contains 90% (cf. J24) of all GCs in UDGs only works well for a GC system with $R_h \approx 2$ kpc. A deviance of 1 kpc from $R_h \approx 2$ kpc leads to notable biases of N_{GC} . However, the effect is not as significant as that from inaccurate assumptions of the GCLF as observed in Figure 7(b). We did not investigate the effect of changing R_h under MATHPOP due to computational constraints, but given that we are also inferring R_h from data, MATHPOP should also work well with differing R_h .

We also used the simulation results to investigate the relationship between the probability that a UDG has no GC ($\mathbb{P}(N_{\text{GC}} = 0)$) and the true value of N_{GC} based on our simulations. We found that the previously selected cutoff probability value of 5% corresponds well to when we consider a UDG to have no GC: for $\mathbb{P}(N_{\text{GC}} = 0) > 5\%$, it roughly coincides with the true N_{GC} being around $1 \sim 2$. For such a low value, it is effectively not possible for any method to distinguish them from being zero or positive.

4.4.2. GC counts versus GCLF

Figure 7(c) shows the relationship between the average posterior mode of N_{GC} ($\bar{N}_{\text{GC}}^{\text{mode}}$) and the posterior mode distributions of μ_{TO} ($\mu_{\text{TO}}^{\text{mode}}$) based on 150 simulations for each parameter configuration of N_{GC} and μ_{TO} . We see that the inferred $\mu_{\text{TO}}^{\text{mode}}$ becomes brighter

as N_{GC} increases, but this is superfluous. Since the prior distribution of μ_{TO} is $\mathcal{N}(26.3, 0.5^2)$, and for low- N_{GC} , the lack of data causes the posterior to be similar to the prior. As N_{GC} increases, $\mu_{\text{TO}}^{\text{mode}}$ gradually approaches the true μ_{TO} since more information becomes available.

Furthermore, for low- N_{GC} , $\mu_{\text{TO}}^{\text{mode}}$ is lower than the mean of the prior distribution at 26.3 mag even if the true μ_{TO} is 26.3 mag. This is because the model has to differentiate whether there are indeed very few GCs or whether the actual μ_{TO} is so faint that most of the GCs are unobserved. Balancing these two options leads to, on average, fainter $\mu_{\text{TO}}^{\text{mode}}$ than its prior mean when N_{GC} is low.

Although the previously observed relationships in Figure 7(c) are not physical, they do tell us, for a given $N_{\text{GC}}^{\text{mode}}$ and a true μ_{TO} , what the possible value of $\mu_{\text{TO}}^{\text{mode}}$ may be. We have plotted in Figure 7(c) the posterior mode estimates (gray points) obtained by our approach of all LSBGs considered in this paper. The relationship between $N_{\text{GC}}^{\text{mode}}$ and $\mu_{\text{TO}}^{\text{mode}}$ for most LSBGs roughly follows the one when the true μ_{TO} is the canonical TO point (red points and confidence bands).

However, for LSBGs R27 and W88, their posterior mode estimates clearly do not obey the relationship observed for the red points and confidence bands. Given their $N_{\text{GC}}^{\text{mode}}$ values, it is statistically nearly impossible to obtain their respective $\mu_{\text{TO}}^{\text{mode}}$ if their true $\mu_{\text{TO}} = 26.3$ mag. In fact, for UDGs with $N_{\text{GC}}^{\text{mode}}$ similar to R27 and W88, a true $\mu_{\text{TO}} = 25.3$ mag, which is a whole magnitude brighter than the canonical TO, is required to have a probable chance of obtaining a $\mu_{\text{TO}}^{\text{mode}}$ similar to R27 and W88. This observation also coincides with the MLEs obtained previously in Section 4.3. Even though the MLEs are only crude estimates, the simulation studies here do suggest that the MLEs should be close to the true values. Therefore, we have sufficient evidence from both real data and simulations that the GCLFs of R27 and W88 are indeed much more weighted toward the luminous end than the canonical GCLF.

The analyses based on our simulation studies demonstrate the accuracy and validity of our approach. Compared to the standard method, our method resolves the issue induced by the variations of the GCLF, which, we show here, is potentially the main driving factor in the massive discrepancy in N_{GC} estimates of UDGs reported in previous studies. Therefore, it is highly important to infer the GCLF from data rather than making assumptions about it. Otherwise, not only N_{GC} estimates of UDGs may be inaccurate, important new discovery about UDGs may also be missed.

5. DISCUSSION AND CONCLUSIONS

In this paper, we have introduced a hierarchical Bayesian mark-dependently thinned point process (MATHPOP) model to infer the GC counts in UDGs and LSBGs in general. Our method has several notable advantages over previous ones.

Firstly, via our approach, we were able to identify two LSBGs (R27 and W88) with GCLFs significantly more weighted to the luminous end than the canonical GCLF, while it is unlikely that the abnormality of these two UDGs would have been discovered under the standard approach. These two new discoveries add toward the samples of UDGs that have abnormal GCLFs and may bring about new understanding of galaxy and GC formation theory. The new discoveries are possible since our approach jointly infers the spatial and magnitude distributions of GCs through a marked point process framework. Under this approach, we not only accurately infer and quantify the uncertainties of GC counts, we can also quantify the GCLF of UDGs in a coherent way without need of making assumptions.

Secondly, under a hierarchical Bayesian point process framework, various uncertainties such as photometric uncertainties and GC membership uncertainties can be fully addressed.

Thirdly, our approach no longer produces GC count estimates or confidence intervals that extend to the negative range. Instead, through simulation studies, we show that the point estimate using the posterior mode under our approach can accurately infer cases of low GC count UDGs. Moreover, our method provides the posterior probability that a UDG has no GC so that proper uncertainty quantification for low GC count UDGs is also available.

Lastly, we provide methods to incorporate the uncertainty associated with GC candidate selection into the entire model fitting procedure while previous methods largely ignored such uncertainties.

While our approach exhibits significant advantages over the standard approach, one main challenge is computation time. Our current MCMC algorithm takes roughly half an hour to run 100 K iterations for data that contains one UDG. For data with more UDGs, the algorithm can take up to hours. Due to the complexity of our model likelihood, much more efficient gradient-based MCMC algorithms such as Hamiltonian Monte-Carlo (Neal et al. 2011) or No-U-Turn sampler (Hoffman et al. 2014) cannot be used. We are currently exploring the possibility of using approximate Bayesian inference with surrogate likelihood or posterior as proposed by (Li & Zhang 2024), which can facilitate fast inference but also provide proper uncertainty quantification.

Another potential issue in this work is that we have not considered realistic simulation of UDGs and their GC systems due to computational constraints. If more computational resources are permitted, more sophisticated software such as ARTPOP (Greco & Danieli 2022) can be used to inject highly realistic simulations of UDGs and their GC populations into real images. Moreover, the uncertainty associated with selection of GC candidates can also be assessed.

Additionally, the problematic results obtained by the probabilistic GC catalog from the J24 point source list should be addressed. Although this is not an inherent problem of our MATHPOP model, it is an integrated part of our entire Bayesian workflow and the quality of data is ultimately the biggest determining factor on the accuracy of the final estimates. However, with only color-magnitude data, it is impossible to confidently separate GCs from contaminants at faint levels for a highly contaminated point source list such as the one in J24. To address this issue, information on how likely a detected source is indeed a point source can be a crucial factor that boosts our ability to separate GCs from contaminants at faint levels.

Overall, this work is an initial step at developing an accurate and robust method to infer and quantify the uncertainty of GC counts in UDGs/LSBGs. There are various directions for future research:

Firstly, we plan to speed up our inference algorithm and apply our method to much larger samples of UDGs/LSBGs from various other catalogs.

Secondly, we will consider extensive simulation studies using the ARTPOP software (Greco & Danieli 2022) to generate realistic UDGs and their GC systems and inject them into real astronomical images. Based on the simulated images, we will conduct the standard data reduction and GC selection step so that all uncertainties associated with data acquisition can be calibrated and assessed under our approach.

Last but not least, we also intend to develop a probabilistic GC classification method where the likelihood that a source is indeed a point source is incorporated. The development of such a method may not only be useful for our problems but can be crucial for various studies relying on catalogs of extra-galactic GCs.

AUTHOR CONTRIBUTION

D.L. contributed to the majority of this work. D.L. conceived the initial idea and proposed the model in the paper. D.L. also wrote majority of the paper and the entire code for model fitting, as well as all the code and analysis to produce all of the figures.

Filter (Camera)	a	$\pm a$	m_0	$\pm m_0$	β_0	$\pm \beta_0$	β_1	$\pm \beta_1$
F814W (ACS)	1.50	0.033	25.75	0.017	0.0884	0.004	0.645	0.015
F475W (ACS)	1.66	0.031	26.93	0.013	0.078	0.003	0.699	0.017
F814W (WFC3)	1.57	0.048	26.52	0.022	0.0977	0.003	0.613	0.011
F475W (WFC3)	1.23	0.040	28.02	0.030	0.0544	0.002	0.652	0.019

Table 4. Estimates of the parameters for the completeness fraction (a, m_0) and the measurement uncertainty function (β_0, β_1), and their uncertainties obtained by artificial fake star tests.

G.M.E. was the PI and co-supervised D.L. G.M.E. provided expertise on Bayesian analysis and astrostatistics. G.M.E. contributed and edited all sections of the paper.

P.E.B. co-supervised D.L. P.B. also provided expertise on statistics and point process models, edited and contributed to Section 3 and Appendix C.

W.E.H. contributed significantly to Section 2 and obtained the initial point source list through DOLPHOT. W.H. also provided expertise on GCs and edited various sections.

R.G.A. co-supervised D.L., and provided expertise on UDGs/LSBGs. R.A. also edited and contributed to Section 1 and 4.

P.V.D. contributed to Section 4 and provided crucial help in paper structure and software construction.

S.R.J. contributed to Section 2, obtained and provided point source list from J24. S.J. also provided expertise on UDGs/LSBGs.

S.C.B. edited and contributed to all sections.

S.D. provided various edits and comments to all sections.

A.J.R. provided various edits and comments to all sections.

J.S. provided crucial help to form the initial idea of the paper and provided expertise on astrostatistics.

ACKNOWLEDGMENTS

Most of the computations in this work were performed using the high performance computing cluster at the Digital Research Alliance of Canada. D.L. would like to acknowledge funding support from Canadian Statistical Sciences Institute and Data Sciences Institute at the University of Toronto through grant number DSI-DSFY2R1P23. W.E.H. would like to acknowledge funding support from NSERC. S.C.B. would like to acknowledge funding support from the Data Sciences Institute at the University of Toronto through grant number DSI-DSFY3R1P24. A.J.R. was supported by National Science Foundation grant AST-2308390.

DATA

All the *HST* raw imaging data used in this paper can be found in MAST: [10.17909/t87p-g529](https://doi.org/10.17909/t87p-g529).

Facilities: *HST*

Software: DOLPHOT, R, Python

APPENDIX

A. ARTIFICIAL STAR TEST RESULTS

Table 4 gives the estimated completeness fraction and the measurement uncertainties in both filters based on our AST.

B. PROBABILISTIC CLASSIFICATION OF GLOBULAR CLUSTERS

B.1. *Our Data*

For our point source data obtained by DOLPHOT, we apply a multivariate nonparametric finite mixture model to obtain the probabilistic GC catalog using the method of Benaglia et al. (2009); Chauveau & Hoang (2016). The method is available in the R package `mixtools` via the function `mvnpEM`. This method requires the least amount of information provided to the algorithm and allows the data itself to facilitate clustering. Specifically, we run the algorithm on 500 simulated color-magnitude distributions, where each simulation is obtained by jittering the color and magnitude of individual point sources using their respective measurement uncertainties. The algorithm is run with the assumption that there are three distinct clusters in the color-magnitude data, where they correspond to (1) the blue star in the

Component	Mixture Weights	Variables	Sub-component Weights	Parameters	Distribution
GCs	w	Magnitude in F814W (mag)	-	$\theta_{\text{GC}}^M = (\mu_{\text{TO}}, \sigma_{\text{GC}})$	$\mathcal{N}(\mu_{\text{TO}}, \sigma_{\text{GC}}^2)$
		Red GCs in F475W – F814W (mag)	w_r	$\theta_{\text{GC,r}}^C = (\mu_{\text{GC,r}}^C, \sigma_{\text{GC,r}}^C)$	$\mathcal{N}(\mu_{\text{GC,r}}^C, (\sigma_{\text{GC,r}}^C)^2)$
		Blue GCs in F475W – F814W (mag)	$1 - w_r$	$\theta_{\text{GC,b}}^C = (\mu_{\text{GC,b}}^C, \sigma_{\text{GC,b}}^C)$	$\mathcal{N}(\mu_{\text{GC,b}}^C, (\sigma_{\text{GC,b}}^C)^2)$
Contaminants	$1 - w$	Magnitude in F814W (mag)	-	$\theta_{\text{cont}} = (\mu_{\text{cont}}, \sigma_{\text{cont}})$	$\mathcal{N}(\mu_{\text{cont}}, \sigma_{\text{cont}}^2)$
		Color in F475W – F814W (mag)	-	-	Unif (0.8, 2.4)

Table 5. Mixture model components and parameters used for clustering point sources from J24 into GCs and contaminants.

lower left corner of the CMD in the left panel of Figure 1, (2) the typical GC candidate region, and (3) the Milky Way foreground stars in the upper right region of the CMD in the left panel of Figure 1. The probability that each source belongs to the cluster representing the GC candidate region is computed.

B.2. J24 Data

For the point source list in J24, the contaminating sources at faint levels are so abundant that the previous nonparametric finite mixture model has difficulties at identifying GC candidates near faint levels. Even within the binary J24 GC catalog, the contaminant populations are still abundant. As a definitive test on the existence of a contaminant population, we follow J24 and assume that sources with $F814W < 26.3$ mag and $0.8 \leq (F475W - F814W) \leq 2.4$ mag are “GCs”. We assume the F814W magnitudes of these “GCs” follow a Gaussian distribution (i.e., the GCLF) that is right-truncated at 26.3 mag. The resulting MLE of μ_{TO} is a non-sensical 43.7 ± 7.75 mag. The inferred μ_{TO} is fainter than the canonical μ_{TO} with 99% confidence and the point estimate of 43.7 mag puts an average “GC” from this catalog outside the observable Universe! This is strong evidence that there is a significant contaminant population among sources brighter than the canonical μ_{TO} . Therefore, we consider a two-component parametric mixture model combined with physical information to aid the clustering. Table provides the list of parameters and model components for our parametric mixture model.

Specifically, we cluster the color-magnitude data with measurement uncertainties considered for sources with $0.8 \leq (F475W - F814W) \leq 2.4$ mag. Suppose that there are n point sources passing the color cuts with magnitude M_i and color C_i , $i \in [n]$. Our two-component mixture model assumes that these sources come from a GCLF component and a contaminant component. We model the magnitude distribution of GCs in these sources using a truncated GCLF with parameter $\theta_{\text{GC}}^M = (\mu_{\text{TO}}, \sigma_{\text{GC}})$, which are respectively the GCLF TO and dispersion. For the color of GCs, we model it by a mixture of two Gaussian distributions that represent the blue and red GCs, each of these components have parameters $\theta_{\text{GC,r}}^C = (\mu_{\text{GC,r}}^C, \sigma_{\text{GC,r}}^C)$ and $\theta_{\text{GC,b}}^C = (\mu_{\text{GC,b}}^C, \sigma_{\text{GC,b}}^C)$. For the contaminant component, we model its magnitude distribution by a Gaussian with parameter $\theta_{\text{cont}} = (\mu_{\text{cont}}, \sigma_{\text{cont}})$, and the color distribution by a uniform distribution in (0.8 mag, 2.4 mag). For simplicity, we assume that the color and magnitude distributions of all components are independent. Denote $\Theta_{\text{mix}} = \{w, w_r, \theta_{\text{GC}}^M, \theta_{\text{GC,r}}^C, \theta_{\text{GC,b}}^C, \theta_{\text{cont}}\}$ Our two-component mixture model is thus:

$$\begin{aligned} \pi(M_i, C_i | \Theta_{\text{mix}}) &= w \pi_{\text{GC}}^M(M_i; \theta_{\text{GC}}^M) \{w_r \pi_{\text{GC,r}}^C(C_i; \theta_{\text{GC,r}}^C) + (1 - w_r) \pi_{\text{GC,b}}^C(C_i; \theta_{\text{GC,b}}^C)\} + \\ &\quad (1 - w) \pi_{\text{cont}}^M(M_i; \theta_{\text{cont}}) \pi_{\text{cont}}^C(C_i) \\ &\triangleq w \pi_{\text{GC}}(M_i, C_i; w_r, \theta_{\text{GC}}^M, \theta_{\text{GC,r}}^C, \theta_{\text{GC,b}}^C) + (1 - w) \pi_{\text{cont}}(M_i, C_i; \theta_{\text{cont}}). \end{aligned} \quad (\text{B1})$$

In the above, $w \in [0, 1]$ is the proportion of GCs, $w_r \in [0, 1]$ is the proportion of GCs that are red. Moreover,

$$\pi_{\text{GC}}^M(M_i; \theta_{\text{GC}}^M) = \frac{\phi(M_i; \mu_{\text{GC}}^M, \sigma_{\text{GC}}^M) f(M_i)}{\int \phi(m; \mu_{\text{GC}}^M, \sigma_{\text{GC}}^M) f(m) dm}, \quad (\text{B2})$$

is the GCLF truncated by the completeness fraction $f(m)$. $\phi(M_i; \mu_{\text{GC}}^M, \sigma_{\text{GC}}^M)$ is the true GCLF of GCs, and we have set $\mu_{\text{GC}}^M = 26.3$ mag (canonical TO), which is the only parameter we fix. For simplicity, we take $f(m)$ to be the average completeness fraction from J24. $\pi_{\text{GC,r}}^C(C_i; \theta_{\text{GC,r}}^C)$ and $\pi_{\text{GC,b}}^C(C_i; \theta_{\text{GC,b}}^C)$ are respectively the Gaussian densities for the color of red and blue GCs. $\pi_{\text{cont}}^M(M_i; \theta_{\text{cont}})$ is the Gaussian density of the magnitude distribution of the contaminants, while $\pi_{\text{cont}}^C(C_i)$ is the uniform color distribution of the contaminants. We then obtain the maximum likelihood estimate

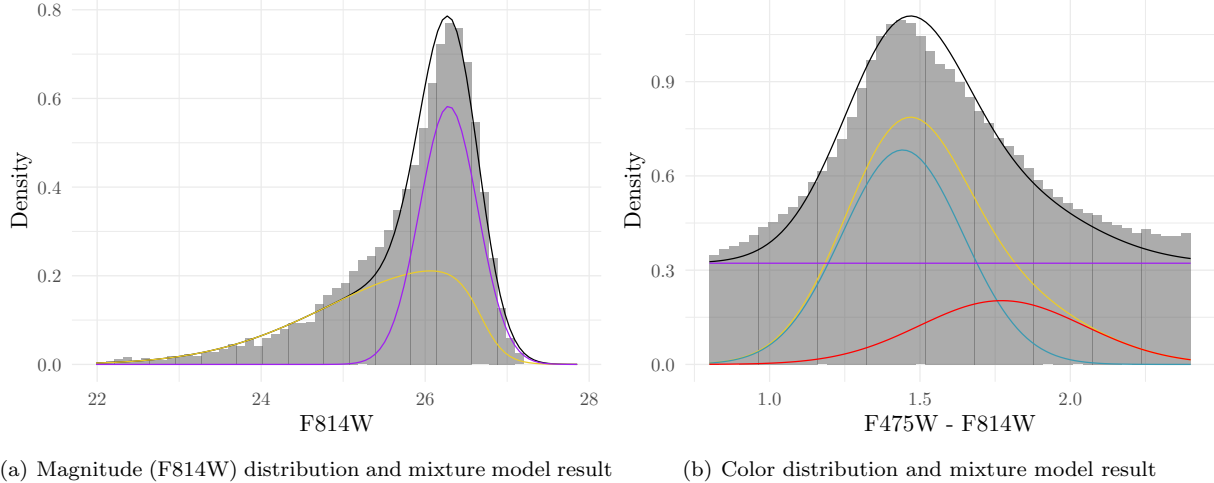


Figure 8. (a) Magnitude and (b) color distribution (grey histograms) of jittered sources from 500 simulations using measurement uncertainties and data from J24. A color cut of $0.8 \leq F475W - F814W \leq 2.4$ is applied to the jittered sources. (a) The black line is the best-fit two-component mixture model for the magnitude distribution of sources. The yellow line is the best-fit truncated GCLF component. The purple line is the best-fit Gaussian distribution for the contaminants component at fainter levels. (b) The black line is the best-fit two-component mixture model for the color distribution of the sources. The yellow line is the best-fit GC color component. The blue and red lines are GC color distributions of blue and red GCs. The purple line is the color distribution of the contaminant. All best-fit lines are the average results from the simulations.

(MLE) of $\hat{\Theta}_{\text{mix}} = \{\hat{w}, \hat{w}_r, \hat{\theta}_{\text{GC}}^M, \hat{\theta}_{\text{GC,r}}^C, \hat{\theta}_{\text{GC,b}}^C, \hat{\theta}_{\text{cont}}\}$. The probability that the i -th source is a GC is then

$$p_{i,\text{GC}} = \frac{\hat{w}\pi_{\text{GC}}(M_i, C_i; \hat{w}_r, \hat{\theta}_{\text{GC}}^M, \hat{\theta}_{\text{GC,r}}^C, \hat{\theta}_{\text{GC,b}}^C)}{\hat{w}\pi_{\text{GC}}(M_i, C_i; \hat{\theta}_{\text{GC}}^M, \hat{\theta}_{\text{GC,r}}^C, \hat{\theta}_{\text{GC,b}}^C) + (1 - \hat{w})\pi_{\text{cont}}(M_i, C_i; \hat{\theta}_{\text{cont}})} \quad (\text{B3})$$

We apply the procedure 500 times to sources that pass the color cuts after jittering the colors and magnitudes of all sources in J24 by their measurement uncertainties.

Figure 8 shows the magnitude and color distributions of the uncertainty jittered sources from the 500 simulations, as well as the best fit mixture model. In both Figures 8(a) and 8(b), the black lines are the best-fit overall two-component mixture results. The yellow lines are the truncated GCLF component, while the purple lines are the contaminant component. In Figure 8(b), the red and blue lines are the respective red and blue GC sub-populations. The mean color estimates are ~ 1.44 mag for blue GCs and ~ 1.77 mag for red GCs, and they are consistent with the estimates in Harris et al. (2020). However, roughly half of the sources with $0.8 \leq (F475W - F814W) \leq 2.4$ mag are contaminant, and most of them have F814W magnitudes fainter than 25.5 mag. Additionally, the contaminant population has the highest density at exactly the canonical GCLF TO point of 26.3 mag. Therefore, it is nearly impossible to separate GCs from contaminants in this region. This is also demonstrated in the right panel of Figure 1 where the probabilities of sources being GCs drop significantly in said region.

As a final note, we also examined the magnitude distribution of our data from DOLPHOT in a similar fashion. We found that there is no significant contaminant population in our data, as the magnitude distribution of sources that pass the color cuts almost coincides exactly with the truncated canonical GCLF. This shows that our catalog is rather clean at fainter levels. In this case, the previous non-parametric finite mixture model will work well at distinguishing GCs.

C. DATA GENERATING PROCESS FOR POINT SOURCES

To incorporate the probabilistic GC catalog into our model, additional structure is required to conduct inference. We denote the extracted point sources with point pattern $\mathbf{x} = \{x_1, \dots, x_n\}$, their magnitudes $\mathbf{M} = \{M_1, \dots, M_n\}$, and their colors $\mathbf{C} = \{C_1, \dots, C_n\}$. Let $\mathbf{Z} = (Z_1, \dots, Z_n)$ be a random vector with $Z_i = 1$ denoting the i -th source is a GC while $Z_i = 0$ being the i -th source is not a GC.

Assume that a data-generating process \mathbb{M}_{GC} with parameters Θ_{GC} gives rise to the GC point pattern \mathbf{x}_{GC} and magnitude \mathbf{M}_{GC} , while another data-generating process \mathbb{M}_{NG} with parameters Θ_{NG} generates point pattern \mathbf{x}_{NG} and magnitude \mathbf{M}_{NG} for sources that are not GCs. We assume that Z_i 's are conditionally independent given the data and model parameters. The full posterior is then

$$\pi(\Theta_{\text{GC}}, \Theta_{\text{NG}}, \mathbf{Z} | \mathbf{x}, \mathbf{M}, \mathbf{C}). \quad (\text{C4})$$

Naturally, the posterior in Eq. C4 can be sampled from the following data-augmentation scheme (van Dyk & Meng 2001; Neal & Kypraios 2015):

1. Sample $\mathbf{Z}' \sim \pi(\mathbf{Z} | \mathbf{x}, \mathbf{M}, \mathbf{C}, \Theta_{\text{GC}}, \Theta_{\text{NG}})$,
2. Sample $\Theta'_{\text{GC}}, \Theta'_{\text{NG}} \sim \pi(\Theta_{\text{GC}}, \Theta_{\text{NG}} | \mathbf{Z}', \mathbf{x}, \mathbf{M})$.

Note that the conditional posterior in Step 2 above does not depend on \mathbf{C} as $(\Theta_{\text{GC}}, \Theta_{\text{NG}})$ are unrelated to the color. However, in Step 1, sampling \mathbf{Z}' requires parametric modelling of the spatial distribution of non-GC point sources and the entire CMD. Such task is extremely difficult since non-GC sources encompass various objects including foreground stars and background galaxies. These non-GC sources have extremely complex distribution and it is simply impossible to parametrically model both their spatial distributions and CMDs.

One key observation is that if we know the nature of each point source, i.e., \mathbf{Z} , the resulting conditional posterior of Θ_{GC} and Θ_{NG} are independent. Thus,

$$\pi(\Theta_{\text{GC}}, \Theta_{\text{NG}} | \mathbf{Z}, \mathbf{x}, \mathbf{M}) = \pi_{\mathbb{M}_{\text{GC}}}(\Theta_{\text{GC}} | \mathbf{Z}, \mathbf{x}, \mathbf{M}) \pi_{\mathbb{M}_{\text{NG}}}(\Theta_{\text{NG}} | \mathbf{Z}, \mathbf{x}, \mathbf{M}), \quad (\text{C5})$$

and we can sample the conditional posterior of $\Theta_{\text{GC}}, \Theta_{\text{NG}}$ separately. Indeed, we do not even require the posterior of Θ_{NG} . However, if we ignore the modeling and sampling of Θ_{NG} , the conditional distribution for \mathbf{Z} is unavailable. Hence, we consider a Bayesian cut model (Plummer 2015; Taborsky et al. 2021), where we introduce additional variables $\mathbf{p}(\mathbf{C}, \mathbf{M}) = \{p(C_i, M_i)\}_{i=1}^n$, on which \mathbf{Z} solely depend, while cutting the dependence of \mathbf{Z} on all other model components:

$$\pi(\mathbf{Z} | \mathbf{x}, \mathbf{M}, \mathbf{C}, \Theta_{\text{GC}}, \Theta_{\text{NG}}) \approx \pi(\mathbf{Z} | \mathbf{p}(\mathbf{C}, \mathbf{M})). \quad (\text{C6})$$

Under such a cut model, we have

$$Z_i \sim \text{Bernoulli}(p(C_i, M_i)), \quad (\text{C7})$$

where $p_i = p(C_i, M_i)$ is the probability that the i -th source is a GC. $\mathbf{p}(\mathbf{C}, \mathbf{M})$ is then determined by the finite-mixture models fitted to the CMD shown in Figure 1. Thus, inference is facilitated through the following adjusted data-augmentation scheme:

1. Sample $\mathbf{Z}' \sim \pi(\mathbf{Z} | \mathbf{p}(\mathbf{C}, \mathbf{M}))$,
2. Sample $\Theta'_{\text{GC}} \sim \pi_{\mathbb{M}_{\text{GC}}}(\Theta_{\text{GC}} | \mathbf{Z}', \mathbf{x}, \mathbf{M})$.

Note that the spatial information \mathbf{x} of point sources is not utilized to inform the nature of point source as it may introduce selection bias. For example, in Carlsten et al. (2022), they deemed sources close to a galaxy are more likely to be GCs. However, as seen in Li et al. (2022, 2024); van Dokkum et al. (2024) with the discovery of potentially dark galaxies such as CDG-1 and CDG-2, it is entirely possible that GCs can belong to almost dark galaxies that were not discovered yet. Thus, considering the spatial distribution of point sources and their proximity to known galaxies can bias the classification results.

D. PRIORS

We now outline the prior distributions for the model parameters. For the mean count of GCs, λ_g , in elliptical galaxies, we assign an informative prior as follows:

$$\log(\lambda_g) \sim \mathcal{N}(\log(N_{\text{SF}}^g), 0.25^2).$$

Here, N_{SF}^g is determined using specific frequency (S_N) relations (Harris 1991):

$$S_N = N_{\text{GC}} 10^{0.4(M_V + 15)}.$$

S_N represents the specific frequency, and N_{GC} is the number of GCs in the galaxy. For this study, we set $S_N = 2$, a value expected for typical elliptical galaxies (Harris 1991). The standard deviation of 0.25 serves as an appropriate representation of the uncertainty observed in GC counts.

For UDGs and LSBGs, we assume a weakly-informative folded Gaussian distribution for λ_u :

$$\lambda_u \sim \text{f}\mathcal{N}(0, 50^2),$$

A folded Gaussian distribution is obtained by taking absolute value of a Gaussian random variable. The standard deviation of 50 signifies the currently observed upper bound of ~ 100 GCs in UDGs.

For half-number radii (R_h^g) of GC systems in elliptical galaxies, we leverage a relationship obtained from Forbes et al. (2017). This relationship links the half-number radius of GC systems in elliptical galaxies to their half-light radius, R_e^g . Specifically, it follows that $R_h \sim 3.7R_e$. R_e^g of bright elliptical galaxies from our data is obtained through SExtractor (Bertin & Arnouts 1996; Li et al. 2022). Therefore, we assign the following log-normal prior to R_h^g :

$$\log(R_h^g)(\log(\text{kpc})) \sim \mathcal{N}(\log(3.7R_e^g), 0.25^2).$$

The choice of a standard deviation of 0.25 in the above equation appropriately represents the observed uncertainty associated with this relationship.

For R_h^u of UDG or LSBG GC system, previous studies have found that $R_h^u \sim 0.8R_e^u - 1.5R_e^u$ with R_e^u the half-light radius of a UDG (van Dokkum et al. 2017; Lim et al. 2018; Saifollahi et al. 2022). Thus, we set

$$\log(R_h^u)(\text{kpc}) \sim \mathcal{N}(\log(R_e^u), 0.5^2).$$

The values of R_e^u for all LSBGs in our data follow from J24. There are a few LSBGs that do not have an estimated half-light radius from J24 due to their small size or faintness. For these ones, we simply set $R_e^u = 1.5$ kpc.

For the Sérsic index, we prescribe the following prior distributions: For elliptical galaxies:

$$\log(\alpha_g) \sim \mathcal{N}(\log(0.5), 0.5^2).$$

For UDGs:

$$\log(\alpha_u) \sim \mathcal{N}(\log(1), 0.75^2).$$

Since all galaxies analyzed in our dataset fall within the lower-mass spectrum, their GC systems generally exhibit smaller Sérsic indices when compared to the most massive giant elliptical galaxies, which can exhibit Sérsic indices exceeding 4.

For the parameters μ_{TO}^k and σ_k of the GCLF, we assign the following prior distributions:

$$\mu_{\text{TO}}^k(\text{mag}) \sim \mathcal{N}(26.3, 0.5^2)$$

and

$$\log(\sigma_k)(\text{mag}) \sim \mathcal{N}(\log(1.3), 0.25^2).$$

The TO point of the GCLF μ_{TO}^k is given a Gaussian prior with mean centered at the canonical GCLF TO of 26.3 mag (Harris et al. 2020, J24) and standard deviation of 0.5 mag. The provided standard deviation is intentionally set to a larger value to allow for potential variation of the GCLF TO in UDGs. The GCLF dispersion is given a log-normal distribution with mode at 1.2 mag, which is also the dispersion of the canonical GCLF (cf. Harris et al. 2020).

Lastly, for the background GC intensity λ_0 , we assign it a log-normal distribution as follows:

$$\log(\lambda_0) \sim \mathcal{N}(\log(\ell_0), 0.4^2).$$

The value of ℓ_0 is image dependent: we determine ℓ_0 by first subtracting the number of GCs in galaxies (assumed as the prior median of λ_k) from the total number of GCs in an image, ensuring it roughly coincides with physical reality. We then obtain a final value of ℓ_0 by accounting for unobserved GCs using the canonical GCLF. The standard deviation of 0.4 is selected to accommodate the substantial uncertainty associated with this process.

E. COMPUTATION AND INFERENCE

To conduct inference for our model, we employ an adaptive MCMC (Haario et al. 2001; Roberts & Rosenthal 2009) algorithm in conjunction with a data-augmentation scheme (van Dyk & Meng 2001; Backlund 2017).

Following Section C, we incorporate a data-augmentation scheme to facilitate inference with \mathbf{Z} being the auxiliary variable. We then generate Θ based on $\pi(\Theta | \mathbf{Z}, \mathbf{x}, \mathbf{M})$ using an adaptive MCMC algorithm.

For the adaptive MCMC transition kernel $p(\cdot | \Theta_i)$, we consider the following

$$\Theta_{i+1} | \Theta_i \sim \begin{cases} \mathcal{N}(\Theta_i, C_\theta) & i \leq 1000, \\ \mathcal{N}(\Theta_i, \gamma \text{Cov}(\{\Theta_j\}_{j=1}^i)) & i > 1000, \end{cases} \quad (\text{E8})$$

C_θ here is a diagonal matrix and $\gamma > 0$ is a scaling parameter. For different images, C_θ is different and fine-tuned. Following (Haario et al. 2001; Roberts & Rosenthal 2009), the optimal value of γ is set to $\gamma = 2.38^2 / \text{dim}(\Theta)$. Note that the parameters in Eq. E8 are transformed so the proposed values would not cause issues in computing the model likelihood.

REFERENCES

Abraham, R. G., & van Dokkum, P. G. 2014, PASP, 126, 55, doi: [10.1086/674875](https://doi.org/10.1086/674875)

Amorisco, N. C., Monachesi, A., Agnello, A., & White, S. D. M. 2018, MNRAS, 475, 4235, doi: [10.1093/mnras/sty116](https://doi.org/10.1093/mnras/sty116)

Backlund, G. 2017

Bastian, N., Pfeffer, J., Kruijssen, J. D., et al. 2020, Monthly Notices of the Royal Astronomical Society, 498, 1050

Benaglia, T., Chauveau, D., & Hunter, D. R. 2009, J Comput Graph Stat, 18, 505, doi: [10.1198/jcgs.2009.07175](https://doi.org/10.1198/jcgs.2009.07175)

Berek, S. C., Eadie, G. M., Speagle, J. S., & Harris, W. E. 2023, The Astrophysical Journal, 955, 22

Bertin, E., & Arnouts, S. 1996, AAPS, 117, 393, doi: [10.1051/AAS:1996164](https://doi.org/10.1051/AAS:1996164)

Bürkner, P.-C., Gabry, J., Kay, M., & Vehtari, A. 2023, posterior: Tools for Working with Posterior Distributions. <https://mc-stan.org/posterior/>

Buzzo, M. L., Forbes, D. A., Jarrett, T. H., et al. 2024, Monthly Notices of the Royal Astronomical Society, 529, 3210, doi: [10.1093/mnras/stae564](https://doi.org/10.1093/mnras/stae564)

Carlsten, S. G., Greene, J. E., Beaton, R. L., & Greco, J. P. 2022, ApJ, 927, 44, doi: [10.3847/1538-4357/ac457e](https://doi.org/10.3847/1538-4357/ac457e)

Chauveau, D., & Hoang, V. T. L. 2016, CSDA, 103, 1, doi: <https://doi.org/10.1016/j.csda.2016.04.013>

Chen, Y., & Gnedin, O. Y. 2023, Monthly Notices of the Royal Astronomical Society, 522, 5638

Danieli, S., van Dokkum, P., Abraham, R., et al. 2020, ApJL, 895, L4, doi: [10.3847/2041-8213/ab8dc4](https://doi.org/10.3847/2041-8213/ab8dc4)

Danieli, S., van Dokkum, P., Trujillo-Gomez, S., et al. 2021, ApJL. <https://arxiv.org/abs/2111.14851>

Danieli, S., van Dokkum, P., Trujillo-Gomez, S., et al. 2022, ApJL, 927, L28, doi: [10.3847/2041-8213/ac590a](https://doi.org/10.3847/2041-8213/ac590a)

De Souza, R. d. S., Hilbe, J., Buelens, B., et al. 2015, Monthly Notices of the Royal Astronomical Society, 453, 1928

Dolphin, A. 2016, DOLPHOT: Stellar photometry, Astrophysics Source Code Library, record ascl:1608.013

Dolphin, A. E. 2000, PASP, 112, 1383, doi: [10.1086/316630](https://doi.org/10.1086/316630)

Eadie, G. M., Harris, W. E., & Springford, A. 2022, ApJ, 926, 162, doi: [10.3847/1538-4357/ac33b0](https://doi.org/10.3847/1538-4357/ac33b0)

El-Badry, K., Quataert, E., Weisz, D. R., Choksi, N., & Boylan-Kolchin, M. 2019, Monthly Notices of the Royal Astronomical Society, 482, 4528

Erwin, P. 2015, The Astrophysical Journal, 799, 226

Fan, M., Wang, J., Kashyap, V. L., et al. 2023, AJ, 165, 66, doi: [10.3847/1538-3881/aca478](https://doi.org/10.3847/1538-3881/aca478)

Ferré-Mateu, A., Gannon, J. S., Forbes, D. A., et al. 2023, Monthly Notices of the Royal Astronomical Society, 526, 4735, doi: [10.1093/mnras/stad3102](https://doi.org/10.1093/mnras/stad3102)

Forbes, D. A., Alabi, A., Romanowsky, A. J., Brodie, J. P., & Arimoto, N. 2020, MNRAS, 492, 487, doi: [10.1093/MNRAS/STAA180](https://doi.org/10.1093/MNRAS/STAA180)

Forbes, D. A., Forbes, & A. D. 2017, MNRAS, 472, L104, doi: [10.1093/MNRASL/SLX148](https://doi.org/10.1093/MNRASL/SLX148)

Forbes, D. A., & Gannon, J. 2024, Monthly Notices of the Royal Astronomical Society, 528, 608

Forbes, D. A., Gannon, J., Couch, W. J., et al. 2019, AAP, 626, A66, doi: [10.1051/0004-6361/201935499](https://doi.org/10.1051/0004-6361/201935499)

Gómez, M., Richtler, T., Infante, L., & Drenkhahn, G. 2001, A&A, 371, 875, doi: [10.1051/0004-6361:20010457](https://doi.org/10.1051/0004-6361:20010457)

Greco, J. P., & Danieli, S. 2022, The Astrophysical Journal, 941, 26

Haario, H., Saksman, E., & Tamminen, J. 2001, Bernoulli, 7, 223. <http://www.jstor.org/stable/3318737>

Harris, W. E. 1991, ARA&A, 29, 543, doi: [10.1146/ANNUREV.AA.29.090191.002551](https://doi.org/10.1146/ANNUREV.AA.29.090191.002551)

—. 2023, ApJ, 265, 9, doi: [10.3847/1538-4365/acab5c](https://doi.org/10.3847/1538-4365/acab5c)

Harris, W. E., Blakeslee, J. P., Whitmore, B. C., et al. 2016, ApJ, 817, 58, doi: [10.3847/0004-637X/817/1/58](https://doi.org/10.3847/0004-637X/817/1/58)

Harris, W. E., Harris, G. L., & Hudson, M. J. 2015, The Astrophysical Journal, 806, 36, doi: [10.1088/0004-637x/806/1/36](https://doi.org/10.1088/0004-637x/806/1/36)

Harris, W. E., Harris, G. L. H., & Alessi, M. 2013, ApJ, 772, 82, doi: [10.1088/0004-637X/772/2/82](https://doi.org/10.1088/0004-637X/772/2/82)

Harris, W. E., Morningstar, W., Gnedin, O. Y., et al. 2014, ApJ, 797, 128, doi: [10.1088/0004-637X/797/2/128](https://doi.org/10.1088/0004-637X/797/2/128)

Harris, W. E., Brown, R. A., Durrell, P. R., et al. 2020, ApJ, 890, 105, doi: [10.3847/1538-4357/ab6992](https://doi.org/10.3847/1538-4357/ab6992)

Hoffman, M. D., Gelman, A., et al. 2014, J. Mach. Learn. Res., 15, 1593

Hu, W., Barkana, R., & Gruzinov, A. 2000, Phys. Rev. Lett., 85, 1158, doi: [10.1103/PHYSREVLETT.85.1158](https://doi.org/10.1103/PHYSREVLETT.85.1158)

Hudson, M. J., Harris, G. L., & Harris, W. E. 2014, The Astrophysical Journal, 787, L5, doi: [10.1088/2041-8205/787/1/l5](https://doi.org/10.1088/2041-8205/787/1/l5)

Hui, L., Ostriker, J. P., Tremaine, S., & Witten, E. 2017, Phys. Rev. D, 95, 043541, doi: [10.1103/PHYSREVD.95.043541](https://doi.org/10.1103/PHYSREVD.95.043541)

Janssens, S. R., Abraham, R., Brodie, J., Forbes, D. A., & Romanowsky, A. J. 2019, ApJ, 887, 92, doi: [10.3847/1538-4357/ab536c](https://doi.org/10.3847/1538-4357/ab536c)

Janssens, S. R., Romanowsky, A. J., Abraham, R., et al. 2022, Monthly Notices of the Royal Astronomical Society, 517, 858871, doi: [10.1093/mnras/stac2717](https://doi.org/10.1093/mnras/stac2717)

Kass, R. E., & Raftery, A. E. 1995, JASA, 90, 773, doi: [10.1080/01621459.1995.10476572](https://doi.org/10.1080/01621459.1995.10476572)

Kissler-Patig, M., Richtler, T., Storm, J., & Valle, M. D. 1997, A&A, 327, 503

Li, D., & Barmby, P. 2021, MNRAS, 501, 3472, doi: [10.1093/mnras/staa3908](https://doi.org/10.1093/mnras/staa3908)

Li, D., Stringer, A., Brown, P. E., Eadie, G. M., & Abraham, R. G. 2024. <https://arxiv.org/abs/2302.06567>

Li, D., & Zhang, Z. 2024, arXiv preprint arXiv:2403.12250

Li, D. D., Eadie, G. M., Abraham, R., et al. 2022, ApJ, 935, 3, doi: [10.3847/1538-4357/AC7B22](https://doi.org/10.3847/1538-4357/AC7B22)

Lim, S., Peng, E. W., Côté, P., et al. 2018, ApJ, 862, 82, doi: [10.3847/1538-4357/AACB81](https://doi.org/10.3847/1538-4357/AACB81)

Lim, S., Côté, P., Peng, E. W., et al. 2020, ApJ, 899, 69, doi: [10.3847/1538-4357/ABA433](https://doi.org/10.3847/1538-4357/ABA433)

Makowski, D., Ben-Shachar, M. S., & Lüdecke, D. 2019, JOSS, 4, 1541, doi: [10.21105/joss.01541](https://doi.org/10.21105/joss.01541)

Martínez-Delgado, D., Läsker, R., Sharina, M., et al. 2016, AJ, 151, 96, doi: [10.3847/0004-6256/151/4/96](https://doi.org/10.3847/0004-6256/151/4/96)

Myllymäki, M. 2009, PhD thesis, Jyväskylä, Finland

Myllymäki, M., & Penttinen, A. 2009, Stat. Neerl., 63, 450, doi: <https://doi.org/10.1111/j.1467-9574.2009.00433.x>

Neal, P., & Kypraios, T. 2015, Statistics and Computing, 25, 333, doi: [10.1007/s11222-013-9435-z](https://doi.org/10.1007/s11222-013-9435-z)

Neal, R. M., et al. 2011, Handbook of markov chain monte carlo, 2, 2

Peng, E. W., & Lim, S. 2016, ApJL, 822, L31, doi: [10.3847/2041-8205/822/2/L31](https://doi.org/10.3847/2041-8205/822/2/L31)

Plummer, M. 2015, Statistics and Computing, 25, 37, doi: [10.1007/s11222-014-9503-z](https://doi.org/10.1007/s11222-014-9503-z)

Roberts, G. O., & Rosenthal, J. S. 2009, J. Comput. Graph. Stat., 18, 349, doi: [10.1198/jcgs.2009.06134](https://doi.org/10.1198/jcgs.2009.06134)

Román, J., Beasley, M. A., Ruiz-Lara, T., & Valls-Gabaud, D. 2019, MNRAS, 486, 823, doi: [10.1093/mnras/stz835](https://doi.org/10.1093/mnras/stz835)

Romanowsky, A. J., Cabrera, E., & Janssens, S. R. 2024, RNAAS, 8, 202, doi: [10.3847/2515-5172/ad7112](https://doi.org/10.3847/2515-5172/ad7112)

Saifollahi, T., Zaritsky, D., Trujillo, I., et al. 2022, MNRAS, 511, 4633, doi: [10.1093/mnras/stac328](https://doi.org/10.1093/mnras/stac328)

Shen, Z., van Dokkum, P., & Danieli, S. 2021, ApJ, 909, 179, doi: [10.3847/1538-4357/abdd29](https://doi.org/10.3847/1538-4357/abdd29)

—. 2023, The Astrophysical Journal, 957, 6, doi: [10.3847/1538-4357/acfa70](https://doi.org/10.3847/1538-4357/acfa70)

Stein, N. M., van Dyk, D. A., Kashyap, V. L., & Siemiginowska, A. 2015, ApJ, 813, 66, doi: [10.1088/0004-637x/813/1/66](https://doi.org/10.1088/0004-637x/813/1/66)

Stetson, P. B. 1987, PASP, 99, 191, doi: [10.1086/131977](https://doi.org/10.1086/131977)

Taborsky, P., Vermue, L., Korzepa, M., & Mrup, M. 2021, IEEE Transactions on Pattern Analysis and Machine Intelligence, 43, 4111, doi: [10.1109/TPAMI.2020.2994396](https://doi.org/10.1109/TPAMI.2020.2994396)

van Dokkum, P., Danieli, S., Abraham, R., Conroy, C., & Romanowsky, A. J. 2019a, ApJ, 874, L5, doi: [10.3847/2041-8213/ab0d92](https://doi.org/10.3847/2041-8213/ab0d92)

—. 2019b, The Astrophysical Journal Letters, 874, L5

van Dokkum, P., Li, D. D., Abraham, R., et al. 2024, Research Notes of the AAS, 8, 135, doi: [10.3847/2515-5172/ad4be6](https://doi.org/10.3847/2515-5172/ad4be6)

van Dokkum, P., Abraham, R., Brodie, J., et al. 2016, ApJL, 828, L6, doi: [10.3847/2041-8205/828/1/L6](https://doi.org/10.3847/2041-8205/828/1/L6)

van Dokkum, P., Abraham, R., Romanowsky, A. J., et al. 2017, ApJL, 844, L11, doi: [10.3847/2041-8213/aa7ca2](https://doi.org/10.3847/2041-8213/aa7ca2)

Van Dokkum, P., Danieli, S., Cohen, Y., et al. 2018, Nature, 555, 629

van Dokkum, P., Wasserman, A., Danieli, S., et al. 2019c, ApJ, 880, 91, doi: [10.3847/1538-4357/ab2914](https://doi.org/10.3847/1538-4357/ab2914)

van Dokkum, P. G., Abraham, R., Merritt, A., et al. 2015, ApJL, 798, 45, doi: [10.1088/2041-8205/798/2/L45](https://doi.org/10.1088/2041-8205/798/2/L45)

van Dyk, D. A., & Meng, X.-L. 2001, *J. Comput. Graph. Stat.*, 10, 1. <http://www.jstor.org/stable/1391021>

Villegas, D., Jordán, A., Peng, E. W., et al. 2010, *ApJ*, 717, 603, doi: [10.1088/0004-637X/717/2/603](https://doi.org/10.1088/0004-637X/717/2/603)

Wang, Q., Peng, E. W., Blakeslee, J. P., et al. 2013, *ApJ*, 769, 145, doi: [10.1088/0004-637X/769/2/145](https://doi.org/10.1088/0004-637X/769/2/145)

Wasserman, A., van Dokkum, P., Romanowsky, A. J., et al. 2019, *ApJ*, 885, 155, doi: [10.3847/1538-4357/ab3eb9](https://doi.org/10.3847/1538-4357/ab3eb9)

Wittmann, C., Lisker, T., Tilahun, L. A., et al. 2017, *MNRAS*, 470, 1512, doi: [10.1093/mnras/stx1229](https://doi.org/10.1093/mnras/stx1229)

Yagi, M., Koda, J., Komiyama, Y., & Yamanoi, H. 2016, *ApJS*, 225, 11, doi: [10.3847/0067-0049/225/1/11](https://doi.org/10.3847/0067-0049/225/1/11)